

1 **Forecasting the North African dust outbreak towards** 2 **Europe in April 2011: A model intercomparison**

3 N. Huneeus^{1,2}, S. Basart³, S. Fiedler^{4*}, J.-J. Morcrette⁵, A. Benedetti⁵, J. Mulcahy⁶, E.
4 Terradellas⁷, C. Pérez García-Pando^{8,9}, G. Pejanovic¹⁰, S. Nickovic^{10,11}, P. Arsenovic^{10,12}, M.
5 Schulz¹³, E. Cuevas¹⁴, J.M. Baldasano^{3,15}, J. Pey^{11,16}, S. Remy^{5#}, B. Cvetkovic¹⁰

6 [1]{Laboratoire de Météorologie Dynamique, IPSL, CNRS/UPMC, Paris, France}

7 [2]{Department of Geophysics and Center for Climate and Resilience Research, University of
8 Chile, Santiago, Chile}

9 [3]{Earth Sciences Department, Barcelona Supercomputing Center, BSC-CNS, Barcelona,
10 Spain}

11 [4]{School of Earth and Environment, University of Leeds, Leeds, UK, now at Karlsruhe
12 Institute of Technology, Institute for Meteorology and Climate Research, Karlsruhe,
13 Germany}

14 [5]{European Centre for Medium-Range Weather Forecasts, Reading, UK}

15 [6]{Met Office, FitzRoy Road, Exeter, EX1 3PB, UK}

16 [7]{Meteorological State Agency of Spain (AEMET), Barcelona, Spain}

17 [8]{NASA Goddard Institute for Space Studies, New York, USA}

18 [9]{Department of Applied Physics and Applied Math, Columbia University, New York,
19 USA}

20 [10]{National Hydrometeorological Service, Belgrade, Serbia}

21 [11]{Institute of Environmental Assessment and Water Research, Spanish Research Council,
22 Barcelona, Spain}

23 [12]{Institute for Atmospheric and Climate Science, ETH, Zürich, Switzerland}

24 [13]{Norwegian Meteorological Institute, Oslo, Norway}

25 [14]{Izaña Atmospheric Research Center, State Meteorological Agency of Spain (AEMET),

26 Santa Cruz de Tenerife, Spain}
27 [15]{Environmental Modelling Laboratory, Technical University of Catalonia, Barcelona,
28 Spain}
29 [16]{Geological Survey of Spain (IGME), Zaragoza, Spain}
30 [*]{Now at Max-Planck Institute for Meteorology, Hamburg, Germany}
31 [#]{Now at Laboratoire de Météorologie Dynamique, IPSL, CNRS/UPMC, Paris, France}
32 Correspondence to: N. Huneus, nhuneus@dgf.uchile.cl
33

34 **Abstract**

35 In the framework of the World Meteorological Organisation's Sand and Dust Storm
36 Warning Advisory and Assessment System, we evaluated the predictions of five state-of-the-
37 art dust forecast models during an intense Saharan dust outbreak affecting Western and
38 Northern Europe in April 2011. We assessed the capacity of the models to predict the
39 evolution of the dust cloud with lead-times of up to 72 hours using observations of aerosol
40 optical depth (AOD) from the Aerosol Robotic Network (AERONET) and the Moderate
41 Resolution Imaging Spectroradiometer (MODIS), and dust surface concentrations from a
42 ground-based measurement network. In addition, the predicted vertical dust distribution was
43 evaluated with vertical extinction profiles from the Cloud and Aerosol Lidar with Orthogonal
44 Polarization (CALIOP). To assess the diversity in forecast capability among the models, the
45 analysis was extended to wind field (both surface and profile), synoptic conditions, emissions
46 and deposition fluxes. Models predict the onset and evolution of the AOD for all analysed
47 lead-times. On average, differences among the models are larger than differences among lead-
48 times for each individual model. In spite of large differences in emission and deposition, the
49 models present comparable skill for AOD. In general, models are better in predicting AOD
50 than near-surface dust concentration over the Iberian Peninsula. Models tend to underestimate

51 the long-range transport towards Northern Europe. Our analysis suggests that this is partly
52 due to difficulties in simulating the vertical distribution dust and horizontal wind. Differences
53 in the size distribution and wet scavenging efficiency may also account for model diversity in
54 long-range transport.

55 **1 Introduction**

56 Desert dust, the largest contributor to the global aerosol burden after sea salt (*Textor et al.*,
57 2006; *Huneus et al.*, 2013), plays an important role in the climate system, the chemical
58 composition of the atmosphere (e.g. *Sokolik et al.*, 2001; *Tegen*, 2003; *Balkanski et al.*, 2007;
59 *Bauer and Koch*, 2005) and the ocean biogeochemical cycles (*Jickells et al.*, 2005; *Aumont et*
60 *al.*, 2008, *Mahowald et al.*, 2009; *Schulz et al.*, 2012; *Gallissai et al.*, 2014). Besides their
61 climate effect, dust aerosols degrade air quality over large regions of the globe (e.g. *Kim et*
62 *al.*, 2001; *Ozer et al.*, 2007; *Querol et al.*, 2009; *Pey et al.*, 2013) and often disproportionately
63 reduce visibility close to source regions, impacting transportation (road vehicles and airports),
64 military operations and photovoltaic energy production (e.g. *Schroedter-Homscheidt et al.*,
65 2013). Some evidence exists for increased mortality when dust aerosols are present in
66 particulate matter with radius smaller than 10 μm (PM10) (*Jiménez et al.*, 2010; *Karanasiou*
67 *et al.*, 2012), and dust storms have been associated to epidemics of meningococcal meningitis
68 in the African Sahel (*Agier et al.*, 2013; *Pérez García-Pando et al.*, 2014a,b).

69

70 The wide variety of impacts along with the importance of dust for weather forecasting (*Pérez*
71 *et al.*, 2006a) have motivated the development of operational forecasting capabilities to
72 predict the occurrence of dust storms (*Benedetti et al.*, 2014). Moreover, the European Union
73 directives establish that model results can be used to determine whether PM10 exceedances
74 are caused by advection of dust or by local pollution. Considering the financial implications
75 of this, there is motivation for atmospheric composition forecast models to improve their
76 performance related to dust. At present, a number of global and regional dust forecast systems
77 are available (e.g. *Woodward*, 2001; *Morcrette et al.*, 2008; 2009; *Pérez et al.*, 2011; *Basart et*
78 *al.*, 2012; *Zhou et al.*, 2008; *Vogel et al.*, 2009). An important limitation for the advancement

79 of operational dust storm forecasts is the lack of standardized evaluation processes, suitable
80 observations and a poorly developed verification system compared to numerical weather
81 prediction (NWP). While NWP benefits from advanced near-real time observations systems
82 and well-established protocols for the evaluation of forecast products, similar procedures for
83 aerosol forecasting are at their beginning (*Reid et al.*, 2010; 2011).

84
85 Recently two international programs for model intercomparison and observation of dust
86 storms emerged: the Sand and Dust Storm Warning Advisory and Assessment System (SDS-
87 WAS) led by the World Meteorological Organization (WMO, <http://www.wmo.int/sdswas>)
88 and the International Cooperative for Aerosol Prediction (ICAP) initiative
89 (<http://icap.atmos.und.edu/>). The SDS-WAS seeks to achieve a comprehensive, coordinated
90 and sustained observations and modelling capacity for sand and dust storms (*Terradellas et*
91 *al.*, 2013). The overall aims are the monitoring of these events, increase the understanding of
92 the dust processes and enhance the dust prediction capabilities. SDS-WAS is organized
93 around two regional nodes, managed by Regional Centres (RC), namely the Northern Africa-
94 Middle East-Europe Regional Centre (NAMEE) hosted by Spain (<http://sds-was.aemet.es/>),
95 and the Asian Regional Centre hosted by China (<http://www.sds.cma.gov.cn/>). Each one of
96 these nodes focuses on sand and dust storms within their region of action. More recently the
97 ICAP (<http://icap.atmos.und.edu/>) was started. This international forum involves multiple
98 centres delivering global aerosol forecast products and seeks to respond to specific needs
99 related to global aerosol forecast evaluation (*Benedetti et al.*, 2011). In contrast to SDS-WAS,
100 this cooperative does not focus exclusively on dust but investigates forecast capabilities of all
101 aerosol species at the global scale. Dust prediction is, however, an important component of
102 the aerosol prediction activities.

103

104 Multiple studies have evaluated the model performance to simulate a given dust event (e.g.
105 *Pérez et al.*, 2006b; *Heinold et al.*, 2007; *Guerrero-Rascado et al.*, 2009; *Kalenderski et al.*,
106 2013), yet only a few have analyzed in detail the model capabilities to predict them up to a
107 few days ahead. *Alpert et al.* (2002) use the aerosol index (AI) of the Total Ozone Mapping
108 Spectrometer (TOMS) to initialize a dust prediction system over Israel developed in the
109 framework of the Mediterranean-Israeli Dust Experiment (MEIDEX). *Zhou et al.* (2008)
110 evaluate an operational sand and dust storm forecasting system (CUACE/Dust) for East Asia,
111 while *Shao et al.* (2003) present a real-time prediction system of dust storms in Northeast
112 Asia. These forecasts successfully predict the temporal and spatial evolution of the dust
113 plume, but little effort has been made to systematically examine the predictability of dust
114 transport from Northern Africa to Europe.

115
116 The present work is done within the framework of the SDS-WAS NAMEE node. This RC
117 gathers and coordinates the exchange of forecasts produced by different dust models and
118 conducts regular model inter-comparison and evaluation within its geographical scope. We
119 examine the performance of five state-of-the-art dust forecast models to predict the intense
120 Saharan dust outbreak transporting dust over Western Europe to Scandinavia between 5 and
121 11 April 2011. Studying a single dust event allows to investigate the model skill in predicting
122 the approach of a dust event with a high temporal resolution of a few hours. Each model is
123 compared against a set of observations, namely dust surface concentration, extinction profiles,
124 aerosol optical depth (AOD) at 550 nm, wind at 10 m above ground level (a.g.l.) and profiles
125 of the horizontal wind. This comprehensive inter-comparison of the models reveals strengths
126 and weaknesses of individual dust forecasting systems and provides an assessment of
127 uncertainties in simulating the atmospheric dust cycle at high temporal resolution. The paper
128 is structured as follows. In Sect. 2 the observational data used for the evaluation and the
129 models considered in this work are introduced. In Sect. 3 we describe the intense dust event

130 selected for this study. Results are shown in Sect. 4 and their discussion is provided in Sect. 5.
131 Our conclusions are described in Sect. 6.

132

133 **2 Data and models**

134 The model evaluation focuses on the days of the event, i.e. from the 5 to 11 of April, and uses
135 data over the North African source region and Europe. Figure 1 shows the region of study
136 along with the locations of the observation stations used. The models are evaluated against
137 aerosol optical depth (AOD), vertical profiles of aerosol backscatter and extinction coefficient
138 (Sect. 2.1), dust surface concentrations (Sect. 2.2), wind speed and other meteorological
139 variables relevant for the event (Sec. 2.3). We conduct a statistical analysis, based on 3-hourly
140 data whenever possible and daily data otherwise and we analyse the models' performance to
141 predict the event with lead-times of 24, 48 and 72 hour. A brief description of each of these
142 datasets follows together with a general description of the models used in this work (Sect.
143 2.4).

144

145 **2.1 Aerosol remote sensing**

146 We used AOD observations at 550 nm from 21 Sun photometers operating within the AErosol
147 RObotic NETwork (AERONET; *Holben et al.*, 1998) whose locations are depicted in Figure
148 1. We use quality-assured direct-sun data (Level 2.0) between 440 and 870nm, which contain
149 an uncertainty on the order of 0.01 for AOD under cloud-free conditions.

150

151 Quantitative evaluations of the modelled dust AOD are conducted for dust-dominated
152 conditions; i.e when the Angström exponent (AE) is less or equal to 0.75 (Basart et al., 2009).

153 All data with AE larger than 1.2 are associated to fine anthropogenic aerosols and are

154 considered free of dust. Values of AE between 0.75 and 1.2 are associated with mixed
155 aerosols and are not included in the analysis. The AOD at 550 nm is derived from data
156 between 440 and 870 nm following the Ångström's law. Because AERONET data are
157 acquired at 15-min intervals on average, all measurements within ± 90 min of the models'
158 outputs are used for the 3-hourly evaluation.

159
160 In addition to ground-based observation, we qualitatively compare the modelled dust AOD to
161 satellite-retrieved aerosol distribution from the Moderate Resolution Imaging
162 Spectroradiometer (MODIS) on board the Aqua satellite. We use daily data from the MODIS
163 Level 3 aerosol products from collection 5.1 at $1^\circ \times 1^\circ$ horizontal resolution. The MODIS
164 algorithm over land produces data only for low ground reflectance (i.e. over dark surfaces)
165 leaving dust aerosol over bright deserts undetected (*Remer et al., 2005*). To evaluate the
166 models over deserts we combine the data with the MODIS Aqua Deep Blue product, which
167 provides information over arid and semi-arid areas by employing radiances from the blue
168 channels to enhance the spectral contrast between surface and dust (*Hsu et al., 2004; 2006*).

169
170 In order to examine the predicted vertical profile of dust aerosol, data from the Cloud and
171 Aerosol Lidar with Orthogonal Polarization (CALIOP) sensor on board the Cloud-Aerosol
172 Lidar and Infrared Pathfinder Satellite Observations (CALIPSO) is used. CALIOP is a
173 standard dual-wavelength (532 and 1064 nm) backscatter lidar operating at a polarization
174 channel of 532 nm. It measures high-resolution (1/3 km in the horizontal direction and 30 m
175 in the vertical direction) profiles of the attenuated backscatter of aerosols and clouds at 532
176 and 1064 nm along with polarized backscatter in the visible channel (*Winker et al., 2009*). We
177 use here the version 3.01 of the Level 2 aerosol backscatter and extinction product at 532 nm
178 (i.e. CAL_LID_L2_05kmAPro-Prov-V3-30). This product has a horizontal resolution of 5 km
179 and a vertical resolution of 60-m in the tropospheric region up to 20 km and 180 m above. We

180 focus on 5 and 7 of April. The model profiles are derived applying a bilinear interpolation to
181 the four closest model grid points to the CALIOP overpass. We also applied a linear temporal
182 interpolation between the two closest 3-hourly outputs to the time of the CALIOP
183 observation.

184

185 **2.2 Dust surface concentration**

186 We also compare the forecasts against daily surface African dust concentration of PM10 for a
187 number of Southern European regional background (RB) environments. *Pey et al.* (2013)
188 created a database with daily desert dust PM10 concentrations from 2001 to 2011. We use
189 here 24 stations of this dataset (Fig. 1). Daily contributions of African dust to PM10 were
190 obtained by subtracting the daily RB level from the PM10 concentration of the day of the
191 event (*Escudero et al.*, 2007). The RB concentration is derived from application of the
192 monthly moving 40th percentile to the PM10 time series after a prior extraction of the days
193 with African dust.

194

195 **2.3 Wind data**

196 National Meteorological Services operate networks of manned and automated weather
197 stations that regularly report atmospheric conditions following WMO standards. In particular,
198 surface stations report synoptic observations every 3 or 6 hours through the WMO's Global
199 Telecommunications System. These observations, in combination with upper-air soundings,
200 satellites and other remote-sensing products, are the basis to derive the initialization fields for
201 NWP models. We use wind speed and direction at 10 m above ground from 60 stations within
202 the study region and the vertical profiles of horizontal wind from radiosondes launched daily
203 at 12 UTC at Bachar (2.25°W, 31.5°N) in Algeria (Fig. 1).

204

205 **2.4 Models**

206 The present study uses three regional and two global models that are run in operational
207 forecasting mode at different centres for weather prediction in Europe. The three regional
208 models are BSC-DREAM8b and NMMB/BSC-Dust from the Earth Sciences Department at
209 the Barcelona Supercomputing Center (ES-BSC) and the DREAM8-NMME from the
210 Southeast European Virtual Climate Change Center (SEEVCC) hosted by the Republic
211 Hydrometeorological Service of Serbia. The global models are MetUMTM developed by the
212 UK Met Office and ECMWF/MACC from the European Centre for Medium-Range Weather
213 Forecasts (ECMWF). We evaluated forecasts initialized at 00 UTC with forecast lead-times of
214 24, 48 and 72 hours using model 3-hourly output fields. The research teams at the modelling
215 centres configured their model experiments independently and not necessarily follow the
216 setup of their respectively daily operational forecast. We clarify that although the modelling
217 systems of SEEVCC and ECMWF include the assimilation of AOD, the simulations
218 conducted by these centres for this study did not include this feature. The spatial resolution,
219 domain size, initial and boundary conditions, differ, in addition to the different physical
220 parameterizations implemented in the models. Details on the individual dust forecasting
221 systems and the model configurations evaluated here are summarized in Table 1. All models
222 provide 3-hourly instantaneous emission fluxes.

223 In addition to these five models, we use the Modern-Era Retrospective Analysis for
224 Research and Application (MERRA) from the National Aeronautics and Space
225 Administration (NASA; Rienecker et al., 2011) to evaluate the model performance in
226 reproducing the synoptic-scale conditions of the event. Near-surface winds from MERRA are
227 shown for completeness. A discussion of limitations of winds from re-analysis can be found
228 elsewhere (e.g., Menut, 2008; Fiedler et al., 2013, 2015, Largeron et al., 2015).

229
230

231 **3 Dust Event**

232 The African dust outbreak affected Europe between 5 and 11 April 2011. On 4 April, an
233 upper level trough approached Northwest Africa from the west. Advection of positive
234 vorticity and the flow interaction with the Atlas Mountains favoured cyclogenesis in the
235 mountain lee (not shown). On 5 of April, the cyclone had deepened over the southern
236 Moroccan-Algerian border causing strong winds of more than 20 ms^{-1} at 850 hPa. The
237 associated near-surface winds produced dust mobilization over Algeria (Fig. 1).

238

239 The emitted dust aerosol was subsequently transported northwards and reached the Iberian
240 Peninsula following the cyclonic flow (not shown). On 6 and 7 of April, a ridge of high
241 pressure over France and a cyclone west of the Azores Islands caused south-easterly winds of
242 up to 17 ms^{-1} at 850 hPa to the west of the Iberian Peninsula that advected the dust plume
243 towards the Atlantic Ocean. High pressure built and strengthened over the Iberian Peninsula
244 and Northwest Africa between the 8 and 9 of April. The resulting southerly winds over the
245 Atlantic transported the dust-laden air towards Great Britain. 10 and 11 April were
246 characterized by a ridge over West Europe with strong south-westerly winds over Great
247 Britain, which advected the more diffused dust cloud towards Scandinavia (Fig. 1b).

248

249 **4 Results**

250

251 **4.1 Dust Transport: AOD and PM10**

252 The northward transport of dust was examined by comparing model AOD forecasts with
253 AERONET measurements at three stations located along the path of the dust cloud (Fig. 2)
254 and daily AOD maps from MODIS (Fig. 3 and Figures S01, S02 and S03 in the Supplement).

255 The three AERONET stations are Saada (31.63°N, 8.16°W) in Morocco close to the dust
256 source, Evora (38.57°N, 7.91°W) in Portugal, and Birkenes (58.39°N, 8.25°E) in Norway
257 (Fig. 1, black squares). The AOD in Saada peaked on 6 April and a second and smaller
258 maximum was observed on 9-10 April (Fig. 2). The latter peak corresponds to a dust plume
259 that did not affect the Iberian Peninsula and is therefore omitted in our discussion. The time
260 series in Evora and Birkenes feature sharp AOD increases during the passage of the dust
261 cloud (Fig. 2). In Evora, the AOD increased from nearly 0.2 on 5 April to a about 0.8 on the
262 next day. In Birkenes, the AOD raised from approximately 0.3 on 9 April to roughly 1.1 on 10
263 April (the AOD actually doubled in 10 April between the early morning and the late evening).
264 The dominance of the dust in the AOD is evidenced by the strong decrease of AE to values
265 below 0.6.

266
267 The 24-hour forecasts produced by MetUM, ECMWF/MACC and NMMB/BSC-Dust
268 overestimate the AOD on the 5 April in Saada, and, except for ECMWF/MACC, they
269 underestimate the peak on 6 April. While MetUM reproduces the peak on 6 April,
270 NMMB/BSC-Dust predicts it 6 hrs earlier, BSC-DREAM8b and ECMWF/MACC reproduce
271 it 3 hrs earlier. DREAM8-NMME reproduces the AERONET AOD on 5 April but
272 underestimates it on the following day whereas ECMWF/MACC mostly overestimates the
273 AOD on both days. At Evora, most models overestimate the AOD on 6 April with the
274 exception of NMMB/BSC-Dust and DREAM8-NMME. On 7 April MetUM and
275 ECMWF/MACC mostly overestimate the AOD, while the rest of the models tend to
276 underestimate it. The AOD forecast differs significantly for lead-times of 48 and 72-hour. For
277 example, while the 24-hour ECMWF/MACC forecast overestimates the AOD in Saada on 5
278 and 6 April, the 72-hour forecast mostly underestimates it. Similarly, at Evora, the 24-hour
279 forecast of NMMB/BSC-Dust slightly underestimates the AOD on 6 April whereas the 72-
280 hour forecast markedly overestimates it during the same day. At Birkenes, all models

281 underestimate the AOD on the 10 April regardless of the forecast lead-time, which reflects the
282 models' difficulties to transport dust in high concentrations up north. ECMWF/MACC
283 presents a large spread between the different forecast times. While it features the best
284 performance for the 24 hr forecast, the model skill markedly decreased for the 72 hr forecast.

285

286 The maps of daily MODIS AOD (Fig. 3 and Figures S01, S02 and S03 in the Supplement)
287 illustrate the progression of the dust cloud in agreement with the AERONET observations
288 presented above. We note that in order to minimize the potential bias due to temporal
289 sampling associated to the satellite passage, the modelled AOD is computed as the average of
290 the fields at 12 and 15 UTC. The models reproduce the main transport features, but differ in
291 the magnitude of the simulated AOD. While MetUM, ECMWF/MACC and NMMB/BSC-
292 Dust overestimate the magnitude of the AOD suggested by the observations for the first day,
293 the BSC-DREAM8b and DREAM8-NMME underestimates them roughly by a factor of three
294 throughout the entire period. For all models the difference in AOD compared to MODIS
295 increases daily. While MODIS attributes AODs above 1 to the dust cloud until 9 April, the
296 models generally simulate AODs below 1 from the 6 April onwards. BSC- DREAM8b and
297 DREAM8-NMME forecast lower AODs than observed in northern Europe from the 9 April
298 onward. Similar results are found for each model regardless of the forecast lead times, both in
299 terms of spatial features and magnitude of simulated AOD (Figures S02 and S03 in the
300 Supplement).

301

302 We used the root mean square error (RMS), mean bias, and Pearson correlation coefficient
303 (R) to assess the skill of each model to predict the AERONET AOD and PM10 (Tables 2 to
304 6). To explore the performance along the path of the dust cloud, the different AERONET
305 stations were grouped into Southern, Central and Northern Europe (SE, CE and NE,
306 respectively) as indicated in Fig. 1. The models present similar performance between the

307 different lead-times for all regions and all skill scores (Tables 2 to 4). Overall, the largest
308 differences in scores among the models are obtained in NE underlining the growing model
309 spread away from dust sources. However, the scores are not necessarily deteriorated with
310 increasing distance from the source. Although in most cases the models present better
311 statistics in SE, some have better statistics in NE (e.g ECMWF/MACC). In addition, the
312 models present the best RMS and mean bias in CE. Although MetUM has the best AOD
313 performance in SE in terms of all three statistics, there is no model that outperforms the other
314 ones in all regions and for all forecast lead-times.

315

316 We examine now the model performance to reproduce near-surface dust concentrations. Most
317 stations in the Iberian Peninsula recorded elevated surface dust concentrations from 6 to 9
318 April with values between 10 and 100 $\mu\text{g}/\text{m}^3$ (Fig. 4 and Fig. S04 in the Supplement). MetUM
319 strongly overestimates the observations of near-surface concentration for all days and all
320 stations. ECMWF/MACC overestimates the surface concentrations, but captures the
321 variability between 6 and 9 April better, indicating a more realistic development of the dust
322 cloud over Europe. BSC-DREAM8b overestimates the concentrations at southern stations for
323 all days, while an underestimation is found at northern sites during the first half of the event.
324 Finally, NMMB/BSC-Dust and DREAM8-NMME generally tend to underestimate the
325 observed concentrations between 6 and 9 April. The 48 and 72 hr forecast, although different
326 from the 24 hr forecast, show equivalent features to the 24 hr forecast in reproducing the
327 observed surface concentration as described above (Figures S05 and S06 in the Supplement).

328

329 The near-surface concentration over the Iberian Peninsula is a critical measure for the dust
330 outbreak and is summarized in Table 5. Overall, the models show similar performance in
331 near-surface concentration of dust aerosols regardless of the forecast lead-times. MetUM
332 presents the largest RMS and mean bias among the models for all lead-times while

333 DREAM8-NMME presents the smallest bias but also the smallest correlation and
334 NMMB/BSC-Dust features the largest correlation.

335

336 **4.2 Dust emissions**

337 The atmospheric transport of dust aerosol depends, among other factors, on the amount, time
338 and place of dust emission. In order to give evidence for possible reasons of model
339 differences identified in the previous sections, the spatial and temporal variability of dust
340 emissions from each model at different forecast lead-times between the 4 and 7 April is
341 compared here.

342

343 The models present large diversity in both magnitude and spatial distribution of the daily dust
344 emissions within the active source regions (Fig. 5). Except for NMMB/BSC-Dust, with
345 maximum emissions on 4 April, the emissions peak within the region of interest on 5 April
346 and decrease thereafter. The overall largest emissions on 5 April are forecasted by MetUM
347 and the smallest ones by ECMWF/MACC. The large emissions from the former are consistent
348 with the overestimated AOD at Saada on 5 April shown in Figure 2. MetUM is the only
349 model to present similar results for the different forecast lead times (Figure S07 and S08). The
350 remaining models forecast mostly increasing emissions with increasing lead-time for 6 and 7
351 April. Models ECMWF/MACC and BSC-DREAM8b present both larger emissions for the 72
352 hr forecast than the 24 and 48 hr forecast on 4 April and vice versa for the following day.

353

354 The difference between the largest (MetUM) and the smallest emission (ECMWF/MACC) is
355 of the order of a factor of ten (Fig. 6). This factor is larger than the uncertainty in the annual
356 mean emission from AEROCOM (*Huneus et al.*, 2011) suggesting that emission uncertainty
357 in single events is particularly large. Most models present maximum emissions on 5 April,

358 except NNMB/BSC-Dust on 4 April. ECMWF/MACC and DREAM8-NMME have emission
359 maxima at 15 UTC whereas MetUM and NNMB/BSC-Dust have the peak in emissions at
360 noon and BSC-DREAM8b at 9 UTC. ECMWF/MACC is the only model with a temporal lag
361 with changing forecast lead-times, namely 3 hrs earlier emissions on 4 April and 3 hrs later on
362 6 April in the 72 hr forecast. Furthermore, ECMWF/MACC and BSC-DREAM8b have the
363 largest differences between the lead-times; contrary to the 24 and 48 hr forecast, the 72 hr
364 forecast presents the peak in emissions on 4 April and decreasing emissions thereafter.
365 Although the other models also present differences between the forecast lead-times, these are
366 mostly in terms of magnitude, and are smaller compared to emission differences in
367 ECMWF/MACC.

368

369 **4.3 Vertical dust profiles**

370 The CALIOP observations show for the 5 April a shallow layer concentrating most of the
371 aerosols below 1 km a.g.l. and extending up to 40°N and a second deeper layer between 2 to 9
372 km a.g.l. and between 25°N and 40°N (Fig. 7). This latter area between 25°N and 40°N
373 coincides with the dust cloud from MODIS as well as the aerosol characterization from the
374 CALIOP product (Fig. S09 in the Supplement). This higher plume can be linked to a
375 precedent dust intrusion that began at the end of March and is not further analysed here. For
376 the 7 April, a deep layer of aerosols extends up to 4 km a.g.l. with most aerosols below two
377 km, south of 25°N and mostly above 2 km between 35°N and 40°N. The latter layer is a
378 consequence of the uplift forced by the Atlas mountains (Fig. S09 in the Supplement).

379

380 The models show a large diversity in the 24-hour forecast of extinction coefficient profiles, in
381 particular for the 5 April when the satellite passes over the western margins of the continent
382 and the adjacent Atlantic Ocean. On this day all models simulate a shallow near-surface dust

383 layer over the continent south of 25°N but fail to reproduce the observed northward extension,
384 except the ECMWF model. It shows a dust layer around 1 km a.g.l. but underestimates the
385 intensity. The aerosol layer above 2 km is not simulated by NMMB/BSC-Dust, but visible,
386 with an underestimated depth and height, in the other models. MetUM and ECMWF/MACC
387 limit the vertical extent of the layer to 4 km and show the largest signal centred at 2 km as
388 opposed to 3 km in the observations. Similarly, BSC-DREAM8b and DREAM8-NMME
389 simulate this layer but with even smaller magnitudes.

390

391 On the 7 April the models mostly agree on the vertical distribution of the aerosol layer.
392 Except for BSC-DREAM8b, all models represent the aerosol layer mostly confined within the
393 first 2km up to 40°N and the depth of the uplift north of 40°N is underestimated. BSC-
394 DREAM8b, however, reproduces the depth of the observed layer extending up to 40°N but
395 the depth of the uplift is overestimated and extended to 6 km. Finally, NMMB/BSC-Dust,
396 BSC-DREAM8b and DREAM8-NMME underestimate the observed magnitude of the
397 extinction coefficient, ECMWF/MACC overestimates it, and MetUM simulates values more
398 in agreement with the observations.

399

400

401 **4.4 Inter-comparison of synoptic conditions**

402

403 The synoptic conditions are important for the origin and evolution of the dust cloud. We
404 investigate the model performance to predict the synoptic conditions at mid-day compared to
405 MERRA. Our analysis focuses on the day of dust emission (5 April), transport towards the
406 Atlantic (7 April) and towards Great Britain and Northern Europe (9 April). The inter-
407 comparison of the geopotential height and wind speed analysis at 850 hPa and 500 hPa is

408 shown for each model for the 24 hr forecast in Figures 8 and 9, respectively. The
409 corresponding results for the 48 and 72 hr forecasts are provided in the supplementary
410 material (Figs. S12-S15).

411
412 5 April is characterized by a cyclone over the Atlas Mountains in Morocco at 850 hPa and
413 500 hPa and strong winds around 26 ms^{-1} occurring to the northeast of the cyclone centre at
414 850 hPa and to the east at 500 hPa (Figs. 8 and 9, respectively). On 7 April the cyclone moved
415 westward while the centre of an anticyclone was located over the Celtic Sea at 850 hPa and
416 near the Pyrenees Mountains at 500 hPa. The associated ridge stretches towards North Africa
417 causing southerlies over the Iberian Peninsula and the Atlantic Ocean. The anticyclone at 850
418 hPa weakened on 9 April and was located over the North Sea. Similarly the ridge at 500 hPa,
419 although persistent, also weakened and extended from the North Sea to Western Europe.

420
421 The 24 hr forecasts reproduced the synoptic development. However, they slightly
422 underestimated the strength of the anticyclone on 7 April at 500 hPa and on 9 April at 850
423 hPa. ECMWF/MACC, NMMB/BSC-Dust and BSC-DREAM8b also tended to underestimate
424 the anticyclone strength on 7 April at 850 hPa. In addition, BSC-DREAM8b shows larger
425 wind speeds than suggested by MERRA to the west of the cyclone centre in all forecasts, a
426 feature not produced by any other model.

427
428 The 48 and 72 hr forecasts do not show major differences compared to the 24 hr forecasts.
429 Some small differences are identified, including an additional weakening of the anticyclone at
430 850 hPa with increasing lead-time on 5 April in NMMB/BSC-Dust and on 7 April in MetUM.
431 Similarly, the ECMWF/MACC and NMMB/BSC-Dust show a weakening of the ridge at 500
432 hPa with increasing lead-time. On 7 April, MetUM, NMMB/BSC-Dust and DREAM8-
433 NMME weaken the high pressure at 500 hPa with increasing lead-time while

434 ECMWF/MACC and BSC-DREAM8b strengthen it. These differences in the strength of the
435 ridge illustrate the model uncertainty in synoptic conditions during the northward transport of
436 the dust cloud. This meteorological uncertainty likely affects the model performance in AOD
437 and surface concentrations. More detailed analysis is needed to reveal the mechanisms
438 causing these differences, which is left for future work.

439

440 **4.5 Wind analysis**

441 We evaluated the forecasted surface winds, a key driver for dust emission and thereby a
442 potential source for emission differences amongst the models. We used spatial averages of 3-
443 hourly surface wind observations (red dots in Fig. 1) between 4 and 7 April 2011 (Fig. 10).
444 We followed the same procedure with the models and the MERRA reanalysis by averaging
445 the nearest grid cells to the wind observation sites. An in-depth evaluation of winds for dust
446 emission would require an analysis of the wind distributions, which is outside the scope of the
447 present work.

448

449 The strongest winds occurred on 4 April, reaching a spatial mean of 5 ms^{-1} at 3 UTC and a
450 south-westerly direction (Fig. 10 and S16 in the supplement material). Peak values in this
451 region were associated to the cyclone in the lee of the Atlas Mountains (Section 2) that caused
452 dust emission. At 6 UTC the wind speed suffered a sharp decrease to 2 ms^{-1} and turned to
453 easterly. The winds are mostly easterly thereafter with a southerly component in the
454 afternoons of 5 and 6 April. The magnitude remains mostly similar from 9 UTC on the 4th
455 until 9 UTC on 5 April, after which winds increased their speed until 21 UTC followed by
456 calms conditions until 12 UTC next day. Calm conditions were also observed during the night
457 of 6 April.

458

459 The models initialized 24 hours ahead of the dust event captured the general development of
460 the 10-m wind (Fig. 10); increase of winds on the afternoon of 5 April and decrease on the
461 night of the same day as well as the calm conditions on the night of 6 April. However, except
462 for BSC-DREAM8b, the models mostly overestimate the wind speed throughout the period.
463 Furthermore, the mostly easterly condition of the winds is also captured by all models, but
464 most of them present a stronger meridional (southerly) wind component than the observations
465 in particular on 5 April and most of the next day (Figures S16 and S17 in the supplement
466 material). All models present north-easterly winds at 3 and 6 UTC on 4 April, but BSC-
467 DREAM8b and DREAM8-NMME are the sole models to present northerly wind component
468 from 18 UTC on 4 April until 6 UTC on the next day. Although observations show north-
469 easterly, this only at 6 and 21 UTC on 4 April. Furthermore, no model reproduces the strong
470 winds at 3 UTC on 4 April, neither in terms of magnitude nor in direction. Interestingly,
471 MERRA reanalysis shows similar difficulties to reproduce the observations as the forecasts.
472 Largeron et al. (2015) attributed the overestimation of night-time surface winds of different
473 reanalysis (MERRA one of them) to be linked to overestimation of the turbulent diffusion of
474 the nocturnal dry stable surface layer. This is a common problem of state-of-the-art re-
475 analysis products (Sandu et al., 2013) that can affect dust emission (Fiedler et al., 2013).

476

477 We examine now the model performance to forecast the vertical profile of horizontal winds
478 measured by two daily radiosondes (noon and midnight) at Bachar (2.25°W , 31.5°N) in
479 Algeria (Figure 11) close to the dust source of this event (Figure 1). The closest model
480 gridbox to the station is considered in this analysis. Two different regimes can be identified
481 from the observed profiles. The dust-emitting regime until 7 April is characterized by almost
482 constant southerlies above 1 km a.g.l. and easterlies near the surface in agreement with the
483 cyclone (Section 4.4). The wind speeds generally increase until 5 April and decrease
484 thereafter. Maxima in wind speed around 30 m/s on 5 April are reached in two layers centred

485 approximately around 1.5 and 4 km. The subsequent relatively calm regime is characterized
486 by weaker winds and stronger variability in wind direction with height and time. The
487 following analysis will focus on the first regime given its role in the emission and northward
488 transport of dust during the event.

489

490 All models simulate the dominant southerlies at elevated levels but they do not reproduce the
491 easterlies close to the surface (Figure 11). Furthermore, most models represent the two
492 maxima in wind speed, yet the maximum around 4 km a.g.l. is weaker and found at higher
493 levels than in the observations. The observed wind maximum between 1 and 2 km a.g.l. is
494 poorly forecasted. Except in ECMWF/MACC, this maximum is forecasted 12 hrs prior to the
495 observations. In addition, the performance to reproduce the depth of the layer with strong
496 winds and its duration varies amongst models. The onset is well reproduced by all models and
497 the strong southerlies agree with observations above 3 km, but below this height, most models
498 terminate the strong winds one day earlier compared to the observations. Lead times of 48
499 hours show no large impact for the other models (Fig. S19) whereas for lead times of 72 hrs
500 MetUM and BSC-DREAM8b forecast the maximum around 4 km a.g.l. delayed with respect
501 to the observations (Fig. S20).

502

503 **5 Discussion**

504 The capacity of five models to predict an intense dust event with a lead-time of up to 72 hours
505 was examined. Each model was compared to a set of observations characterizing the dust
506 outbreak from Northwest Africa towards Europe between 5 and 11 April 2011. The focus was
507 to assess the capabilities to predict the evolution of AOD and dust surface concentration along
508 the path of the dust cloud. For the former we compared model outputs to both satellite daily

509 products and ground-based three-hourly observations from the AERONET network whereas
510 for the latter we compared forecasted daily near-surface dust concentration to daily-inferred
511 surface concentration observation. The analysis was extended to wind (both surface and
512 profile), synoptic conditions, aerosol vertical distribution, emissions and deposition fluxes as
513 an attempt to explain the diversity in forecast capability among the models.

514
515 Comparison against MODIS AOD revealed that all models reproduce the main features of the
516 daily AOD horizontal distribution throughout the analysed period. However, MetUM,
517 ECMWF/MACC and NMMB/BSC-Dust overestimate the AOD the first days of the event
518 when the dust cloud is over northern Africa and southern Spain, while BSC-DREAM8b and
519 DREAM8-NMME underestimate it. Yet, analysis against AERONET data at Saada, in
520 northern Africa, show that the AOD is mostly underestimated on the days of maximum AOD.
521 We highlight that, according to the simulations, this station is located on the borders of the
522 dust cloud and therefore the bias of each model with respect to the observations is sensitive to
523 both the magnitude of the emitted dust amount and the position of the dust cloud.

524
525 We note that while the observed AOD, from both AERONET and MODIS, corresponds to the
526 total AOD and is therefore sensitive to all aerosol species, the simulated one corresponds to
527 the optical depth due to dust particles only. The model bias thus could be partly due to
528 excluded aerosol species. However, the low observed AE (<0.3) on days of maximum AOD
529 (Fig. 2) indicate that the particles in the atmospheric column are dominated by large particles.
530 This is particularly evident at sites remote from dust sources. Furthermore, this allows
531 attributing the model performance in its capacity, at least in days with low AE, to simulate the
532 dust event.

533

534 All models agree in underestimating the AOD at Birkenes with respect to both AERONET
535 and MODIS. The underestimation of AOD at Birkenes by models BSC-DREAM8b and
536 DREAM8-NMME is consistent with the underestimation of AOD in northern Africa.
537 However, underestimations by models overestimating the AOD in northern Africa (MetUM,
538 ECMWF/MACC and NMMB/BSC-Dust) suggest that not enough dust is transported
539 northward. This could be associated either to the representation of synoptic conditions
540 affecting the horizontal transport or removal processes in the models.

541

542 A difference in emission of the order of a factor of ten is observed between the models (Fig.
543 6). The individual reasons for the model differences are unknown, but potential sources for
544 differences are discussed in the following. One potential reason for different emission, are the
545 model-dependent emission parameterizations with different particle size distributions.
546 ECMWF/MACC has a size distribution with particles of up to 20 μm in diameter whereas the
547 other four models have maximum sizes of 10 μm (Table 1). However, ECMWF/MACC has
548 the smallest emission. Even for the three models with the same number of bins and the same
549 size distribution (NNMB/BSC-Dust, BSC-DREAM8b and DREAM8-NMME) large emission
550 differences exist pointing to the importance of other aspects. Furthermore, previous studies
551 have shown that dust-emitting winds differ amongst models and can be attributed to the
552 representation of atmospheric processes (e.g., Fiedler et al., 2015). Future studies should
553 examine the detailed differences in winds and size distribution of the emissions, including
554 aspects of model resolution that is crucial to represent different atmospheric processes.
555 Deposition (and its size distribution) should also be examined further in future studies given
556 its importance in model performance to simulate dust concentration and AOD.

557

558 Analysis of the total accumulated daily dust deposition suggests that most of the removal

559 occurs in northern Africa close to the source and little is removed over the Atlantic and
560 Europe (Figs. 12 and S21 and S22 in the Supplement). The absence of observed deposition
561 data prevents assessing this aspect of the models performance. The limited deposition away
562 from the source, indicating a too short dust aerosol lifetime in the models, is in agreement
563 with the underestimated dust layer height and AOD away from North Africa. However,
564 observations taken during the Fennec project (Washington et al., 2012) suggest the presence
565 of large particles in higher levels (Allen et al., 2013; Ryder et al., 2013). This could indicate
566 potential dust deposition further away from the source as illustrated by the models and
567 highlights the role of large particles in removal processes as a potential source of errors. It is
568 interesting that the models with the largest emission are not necessarily the ones with the
569 strongest removal, for instance for the first days of the event NMMB/BSC-Dust, BSC-
570 DREAM8b and DREAM8-NMME present stronger total emissions than ECMWF/MACC but
571 lower deposition fluxes.

572

573 Comparison of synoptic maps at 850 and 500 hPa of each model against MERRA reanalysis
574 show that models reproduce the main circulation patterns at both levels. Larger differences
575 are observed in the representation of the vertical structure of horizontal wind, in particular the
576 onset and duration of the southerly winds and the height of layers with maximum speed. In
577 addition to this, analysis of the vertical structure of the dust cloud reveals that the models
578 generally underestimate the depth and magnitude of the dust layer as suggested by CALIOP
579 observations. We note however, that CALIOP may overestimate the aerosol extinction
580 coefficient in layers with significant mixture of mineral dust and marine aerosols due to an
581 overestimation of the lidar ratio (Cuevas et al., 2014). Nevertheless, both of the before
582 mentioned factors (vertical structure of horizontal wind and vertical dust propagation)
583 combined could contribute to the reduced northward dust transport to Birkenes in the models;

584 dust particles do not reach layers of strong winds responsible for the northward transport.

585

586 The models show, all in all, similar performance to forecast AERONET AOD. In general no
587 model outperforms the other in all statistics and for both variables (AOD and surface
588 concentration) and the inter-model spread is larger than the change in forecast skill with lead-
589 time. While for the near-surface concentration of dust the NMMB/BSC-Dust presents the best
590 performance in term of all statistics, for AOD the best performing model depends on the
591 region and forecast lead-time. We recall the reader that for analysis with AERONET data,
592 stations were grouped into southern (SE), central (CE) and northern Europe (NE), whereas for
593 surface concentration stations were not grouped but considered as part of southern Europe.
594 Furthermore most models present better RMS and mean bias in CE. This suggests that errors
595 are large both close to dust sources and in long-distance transport. In addition, NE presented
596 in some cases better statistics than SE. The reasons for this has not been examined in detail,
597 but could be a consequence of the low AOD in NE including non-dust situations, i.e. the
598 models successfully reproduce the dust free days in northern Europe. For near-surface dust
599 concentration, the different forecast lead-times also show similar performance for each model.
600 As for AOD, overall the difference between models is larger than the differences between
601 lead-times. We note however that these results correspond to only one event and the number
602 of stations used in this statistical analysis is small (21 stations for AOD and 24 for dust
603 surface concentration) with only a few days considered. Therefore, the statistical significance
604 of these results needs to be explored considering multiple events before drawing generalized
605 conclusions.

606

607 We use the mean normalized gross errors (MNGE) to assess the difference between the
608 performance to reproduce AOD and near-surface concentration. This statistic measures the

609 relative difference to the observations and allows comparing two variables with different
610 magnitudes. Consistent with the difficulties of models to reproduce the vertical dust
611 distribution, quantitative assessment of the model performance in AOD and near-surface dust
612 concentration show that models have a better forecast skill for the former independent of the
613 forecasting lead times and station; all show smaller MNGE for the AOD (Table 6).
614 Furthermore, the model diversity to forecast near-surface dust concentration, indicated by the
615 range of MNGE between the models, is much larger than the corresponding range in AOD
616 forecast skill.

617
618 In spite of the large model diversity in magnitude and spatial distribution of the emissions and
619 deposition, models present comparable performance when simulating AOD over Northern
620 Africa and Europe. Although this feature can be likely attributed to the practice in model
621 development using AOD values to tune dust simulations, other reasons cannot be excluded.
622 The AOD depends on both, burden and size distribution of dust particles. Therefore, biases in
623 AOD, in particular in the source region, can be associated to biases in the net fluxes and/or to
624 misrepresentation of the size distribution (*Huneeus et al.*, 2011). In addition, definition of
625 optical parameters is also relevant to determine the scattering efficiency of dust particles in a
626 model, and thus AOD. The present study has focused on the forecast skill of the dust lifecycle
627 (i.e. emission, transport and deposition) of a given event from different models, but has not
628 examined the role of size distribution nor definition of optical parameters in the forecast
629 performance.

630

631 **6 Conclusions**

632 As part of the WMO SDS-WAS five state-of-the-art dust forecast models were examined in

633 their performance to predict an intense Saharan dust outbreak towards Western Europe and
634 Scandinavia between 5 and 11 April 2011. The models are successful in predicting the onset
635 and evolution of the dust cloud in terms of AOD for all three analyzed lead-times, namely 24,
636 48 and 72 hours. Yet all models underestimate the northward transport of dust, in particular
637 by those models overestimating the AOD in the source region. Weaker horizontal winds,
638 layers with maximum wind at higher altitudes than observed and too shallow dust layers
639 simulated by the models might explain why not enough dust is transported northward.
640 Quantitative forecast-skill analysis revealed that in general no model outperforms the other in
641 all statistics. Nevertheless, the choice of model has a larger impact on the forecast skill than
642 the lead-time. Furthermore, and in agreement with the difficulties to reproduce the vertical
643 distribution of dust, the models perform better in forecasting the AOD in the Iberian Peninsula
644 than the near-surface dust concentrations.

645

646 Large diversity exists among the models in their emissions and deposition both in terms of
647 magnitude and spatial distribution. The difference in these fluxes is on the order of a factor
648 ten, exceeding the uncertainty amongst models in the annual mean emission (*Huneeus et al.*,
649 2011). This result underlines the particularly large model uncertainty for an individual dust
650 storm. In light of the perception that cyclones are reasonably well forecasted, e.g. compared to
651 dust storms due to cold pool outflows from tropical convection (e.g. Heinold et al., 2013), this
652 result is even more striking. The models also present large diversity in the timing of the
653 emissions, varying between afternoon, noon and morning. In spite of these large differences,
654 the models have comparable skills to forecast AOD likely due to the use of AOD values to
655 tune dust models.

656

657 The results highlight the need of future studies assessing the performance of dust models to

658 examine individual processes in more detail, particularly the vertical mixing, 3D wind fields,
659 emission/deposition and vertical distribution of dust. These need to be better understood for
660 more robust dust storm forecasting. Emission and deposition need to be further investigated
661 not only in terms of their magnitude but also in terms of spatial distribution. In addition and in
662 spite of the, all in all, successful representation of the synoptic conditions by the different
663 models, the vertical distribution of the horizontal wind and vertical mixing of dust needs to be
664 assessed more extensively. However, we also stress that more observations are needed; the
665 absence of emission and deposition measurements precludes evaluation of the net model
666 fluxes and the current scarcity or lack of routine observations of dust surface concentration,
667 lidar and wind profiles prevent a more detailed assessment of model performance and
668 identifying current sources of bias. Finally, this work has examined the models in their
669 performance for a single event and should be replicated for other events and in other dust
670 source regions before drawing definitive conclusions.

671

672 This study has focused on the dust aerosol lifecycle of the event (i.e. emission, transport and
673 deposition) to examine the forecast skill of each model and the differences in skill among
674 them. We have highlighted the importance of the size distribution to conclude on emissions
675 biases due to biases in AOD. However, the impact of the scattering efficiency on the forecast
676 skill has not been addressed. The AOD depends on burden and size distribution, but definition
677 of optical parameters is also relevant to determine the scattering efficiency of dust particles in
678 a model. We suggest that future intercomparison studies examining the model performance to
679 reproduce the dust lifecycle include explicitly the size distribution in their analysis and
680 comparisons against observations allowing to conclude on the performance to reproduce it
681 (e.g. Angström exponent). In addition, the comparison of definition of optical parameters
682 between the different models should also be incorporated.

683

684 **Acknowledgements**

685 The authors acknowledge AERONET (<http://aeronet.gsfc.nasa.gov>) and thank the PIs of the
686 AERONET stations used in this paper for maintaining the observation program, and the
687 AERONET-Europe TNA (EU-ACTRIS grant no. 262254) for contributing to calibration
688 efforts. We also acknowledge the MERRA, CALIPSO and MODIS mission scientists and
689 associated NASA personnel for the production of the data used in this research effort. MODIS
690 data used in this paper were produced with the Giovanni online data system, developed and
691 maintained by the NASA GES DISC. S. Basart acknowledge the Catalan Government (BE-
692 DGR-2012) as well as the CICYT project (CGL2010-19652 and CGL2013-46736) and
693 Severo Ochoa (SEV-2011-00067) programme of the Spanish Government. The NMMB/BSC-
694 Dust and BSC-DREAM8b simulations were performed on the MareNostrum supercomputer
695 hosted by BSC. Stephanie Fiedler acknowledges the funding of the European Research
696 Council through the starting grant of Peter Knippertz (Number 257543). Nicolas Huneus
697 acknowledges FONDAP 15110009. The database on dust concentrations at ground level was
698 produced in the framework of the Grant Agreement LIFE10 ENV/IT/327 from the LIFE
699 Programme of the European Commission. J. Pey has been partially funded by a Ramon y
700 Cajal Grant (RYC-2013-14159) from the Spanish Ministry of Economy and Competitiveness.
701 Carlos Pérez García-Pando acknowledges the Department of Energy (DE-SC0006713), and
702 the NASA Modeling, Analysis and Prediction Program.

703 **Reference**

704

705

706

707 Allen, C. J. T., R. Washington, and S. Engelstaedter (2013), Dust emission and transport
708 mechanisms in the central Sahara: Fennec ground-based observations from Bordj Badji
709 Mokhtar, June 2011, *J. Geophys. Res. Atmos.*, 118, 6212–6232,
710 doi:10.1002/jgrd.50534.

711 Alpert, P., S. O. Krichak, M. Tsidulko, H. Shafir, and Joseph, J. H.: A Dust Prediction System
712 with TOMS Initialization, *Monthly Weather Review*, 130(9), 2335-2345,
713 doi=10.1175/1520-0493(2002)130<2335:adpswt>2.0.co;2, 2002.

714 Aumont, O., L. Bopp, and Schulz, M.: What does temporal variability in aeolian dust
715 deposition contribute to sea-surface iron and chlorophyll distributions?, *Geophys. Res.*
716 *Lett.*, 35(7), L07607, doi:10.1029/2007GL031131, 2008.

717 Bagnold, R. A.: *The Physics of Blown Sand and Desert Dunes* (p. 320). London: Methuen,
718 1941.

719 Balkanski, Y., M. Schulz, T. Claquin, and Guibert, S.: Reevaluation of Mineral aerosol
720 radiative forcings suggests a better agreement with satellite and AERONET data, *Atmos.*
721 *Chem. Phys.*, 7, 81-95, 2007.

722 Basart, S., C. Perez, S. Nickovic, E. Cuevas, and Baldasano, J. M.: Development and
723 evaluation of the BSC-DREAM8b dust regional model over Northern Africa, the
724 Mediterranean and the Middle East, *Tellus B*, 64, doi=Artn 18539Doi
725 10.3402/Tellusb.V64i0.18539, 2012.

726 Bauer, S. E., and Koch, D.: Impact of heterogeneous sulfate formation at mineral dust
727 surfaces on aerosol loads and radiative forcing in the Goddard Institute for Space
728 Studies general circulation model, *Journal of Geophysical Research: Atmospheres*,
729 110(D17), D17202, doi=10.1029/2005JD005870, 2005.

730 Benedetti, A., J. S. Reid, and Colarco, P. R.: International Cooperative for Aerosol Prediction
731 Workshop on Aerosol Forecast Verification, *Bull. Amer. Meteorol. Soc.*, 92(11), ES48-

732 ES53, doi=10.1175/bams-d-11-00105.1, 2011.

733 Benedetti, A., J.M. Baldasano, S. Basart, F. Benincasa, O.Boucher, M. Brooks, J.-P. Chen,
734 P.R. Colarco, S. Gong, N. Huneus, L. Jones, S. Lu, L. Menut, J.-J. Morcrette, J.
735 Mulcahy, S. Nickovic, C. Pérez, J.S. Reid, T.T. Sekiyama, T.Y. Tanaka, E. Terradellas,
736 D.L. Westphal, X.-Y. Zhang, and Zhou, C.-H.: Numerical prediction of dust, in: Mineral
737 dust – a key player in the Earth system, edited by Peter Knippertz and Jan-Berend Stuut,
738 Dordrecht & Springer , 230-240, 2014.

739 Cuevas, E., Camino, C., Benedetti, A., Basart, S., Terradellas, E., Baldasano, J. M., Morcrette,
740 J.-J., Marticorena, B., Goloub, P., Mortier, A., Berjón, A., Hernández, Y., Gil-Ojeda,
741 M., and Schulz, M.: The MACC-II 2007–2008 reanalysis: atmospheric dust evaluation
742 and characterization over Northern Africa and Middle East, *Atmos. Chem. Phys.*, 15,
743 3991–4024, doi:10.5194/acp-15-3991-2015, 2015.

744 Escudero, M., X. Querol, J. Pey, A. Alastuey, N. Pérez, F. Ferreira, S. Alonso, S. Rodríguez,
745 and Cuevas, E.: A methodology for the quantification of the net African dust load in air
746 quality monitoring networks, *Atmospheric Environment*, 41(26), 5516-5524,
747 doi=http://dx.doi.org/10.1016/j.atmosenv.2007.04.047, 2007.

748 Fecan, F., B. Marticorena, and Bergametti, G.: Parameterization of the increase of the aeolian
749 erosion threshold wind friction velocity due to soil moisture for arid and semi-arid areas,
750 *Ann. Geophys.*, 17(1), 149-157, 1999.

751 Fiedler, S., K. Schepanski, B. Heinold, P. Knippertz, and I. Tegen, Climatology of nocturnal
752 low-level jets over North Africa and implications for modeling mineral dust emission, *J.*
753 *Geophys. Res. Atmos.*, 118, 6100–6121, doi:10.1002/jgrd.50394, 2013.

754 Fiedler, S., P. Knippertz, S. Woodward, G. Martin, N. Bellouin, A. Ross, B. Heinold, K.
755 Schepanski, C. Birch, and I. Tegen, A process-based evaluation of dust-emitting winds
756 in the CMIP5 simulation of HadGEM2-ES, *Clim. Dyn.*, 1–24, doi:10.1007/s00382-015-

757 2635-9, 2015.

758 Gallisai, R., Peters, F., Volpe, G., Basart, S., and Baldasano, J. M.: Saharan Dust Deposition
759 May Affect Phytoplankton Growth in the Mediterranean Sea at Ecological Time Scales,
760 *PloS One*, 9, e110762. doi:10.1371/journal.pone.0110762, 2014.

761 Ginoux, P., M. Chin, I. Tegen, J. M. Prospero, B. Holben, O. Dubovik, and Lin, S. J.: Sources
762 and distributions of dust aerosols simulated with the GOCART model, *J. Geophys. Res.-*
763 *Atmos.*, 106(D17), 20255-20273, 2001.

764 Guerrero-Rascado, J. L., F. J. Olmo, I. Avilés-Rodríguez, F. Navas-Guzmán, D. Pérez-
765 Ramírez, H. Lyamani, and Alados Arboledas, L.: Extreme Saharan dust event over the
766 southern Iberian Peninsula in september 2007: active and passive remote sensing from
767 surface and satellite, *Atmos. Chem. Phys.*, 9(21), 8453-8469, doi=10.5194/acp-9-8453-
768 2009, 2009.

769 Heinold, B., J. Helmert, O. Hellmuth, R. Wolke, A. Ansmann, B. Marticorena, B. Laurent,
770 and Tegen, I.: Regional modeling of Saharan dust events using LM-MUSCAT: Model
771 description and case studies, *Journal of Geophysical Research: Atmospheres*, 112(D11),
772 D11204, doi=10.1029/2006JD007443, 2007.

773 Heinold, B., P. Knippertz, J. H. Marsham, S. Fiedler, N. S. Dixon, K. Schepanski, B. Laurent,
774 and Tegen, I.: The role of deep convection and nocturnal low-level jets for dust emission
775 in summertime West Africa: Estimates from convection-permitting simulations, *J.*
776 *Geophys. Res. Atmos.*, 118, 4385–4400, doi:[10.1002/jgrd.50402](https://doi.org/10.1002/jgrd.50402), 2013.

777 Holben, B. N., T. F. Eck, I. Slutsker, D. Tanre, J. P. Buis, A. Setzer, E. Vermote, J. A.
778 Reagan, Y. J. Kaufman, T. Nakajima, F. Lavenue, I. Jankowiak, and Smirnov, A.:
779 AERONET - A federated instrument network and data archive for aerosol
780 characterization, *Remote Sens. Environ.*, 66(1), 1-16, 1998.

781 Hsu, N. C., Tsay, S. C., King, M. D., and Herman, J. R.: Aerosol properties over bright-

782 reflecting source regions. *IEEE Transactions on Geoscience and Remote Sensing*, *42*,
783 557–569. doi:10.1109/TGRS.2004.824067, 2004.

784 Hsu, N. C., Tsay, S. C., King, M. D., and Herman, J. R.: Deep Blue retrievals of Asian
785 aerosol properties during ACE-Asia. *IEEE Transactions on Geoscience and Remote*
786 *Sensing*, *44*, 3180–3195. doi:10.1109/TGRS.2006.879540, 2006.

787 Huneus, N., M. Schulz, Y. Balkanski, J. Griesfeller, J.A. Prospero, S. Kinne, S. Bauer, O.
788 Boucher, M. Chin, F. Dentener, T. Diehl, R. Easter, D. Fillmore, S. Ghan, P. Ginoux, A.
789 Grini, L. Horowitz, D. Koch, M. Krol, W. Landing, X. Liu, N. Mahowald, R. Miller, J.-
790 J. Morcrette, G. Myhre, J.E. Penner, J. Perlwitz, P. Stier, T. Takemura, and Zender, C.:
791 Global dust model intercomparison in AeroCom phase I, *Atmos. Chem. Phys.*, *11*,
792 7781–7816, doi:10.5194/acp-11-7781-2011, 2011.

793 Huneus, N., O. Boucher, and Chevallier, F.: Atmospheric inversion of SO₂ and primary
794 aerosol emissions for the year 2010, *Atmos. Chem. Phys.*, *13*(13), 6555-6573,
795 doi=10.5194/acp-13-6555-2013, 2013.

796 Iversen, J. D., and White, B. R.: Saltation threshold on Earth, Mars and Venus,
797 *Sedimentology*, *29*, 111-119, 1982.

798 Jickells, T. D., Z. S. An, K. K. Andersen, A. R. Baker, G. Bergametti, N. Brooks, J. J. Cao, P.
799 W. Boyd, R. A. Duce, K. A. Hunter, H. Kawahata, N. Kubilay, J. laRoche, P. S. Liss, N.
800 Mahowald, J. M. Prospero, A. J. Ridgwell, I. Tegen, and R. Torres (2005), Global iron
801 connections between desert dust, ocean biogeochemistry, and climate, *Science*,
802 *308*(5718), 67-71

803 Jiménez, E., C. Linares, D. Martínez, and J. Díaz (2010), Role of Saharan dust in the
804 relationship between particulate matter and short-term daily mortality among the elderly
805 in Madrid (Spain), *Science of The Total Environment*, *408*(23), 5729-5736,
806 doi=http://dx.doi.org/10.1016/j.scitotenv.2010.08.049.

807 Kalenderski, S., G. Stenchikov, and C. Zhao (2013), Modeling a typical winter-time dust
808 event over the Arabian Peninsula and the Red Sea, *Atmos. Chem. Phys.*, *13*(4), 1999-
809 2014, doi=10.5194/acp-13-1999-2013.

810 Karanasiou, A., N. Moreno, T. Moreno, M. Viana, F. de Leeuw, and X. Querol (2012), Health
811 effects from Sahara dust episodes in Europe: Literature review and research gaps,
812 *Environ. Int.*, *47*(0), 107-114, doi=http://dx.doi.org/10.1016/j.envint.2012.06.012.

813 Kim, K. W., Y. J. Kim, and S. J. Oh (2001), Visibility impairment during Yellow Sand
814 periods in the urban atmosphere of Kwangju, Korea, *Atmospheric Environment*, *35*(30),
815 5157-5167

816 LARGERON, Y., F. GUICHARD, D. BOUNIOL, F. COUVREUX, L. KERGOAT, and B. MARTICORENA (2015),
817 Can we use surface wind fields from meteorological reanalyses for Sahelian dust
818 emission simulations? *Geophys. Res. Lett.*, *42*, doi:10.1002/2014GL062938.

819 MAHOWALD, N. M., S. ENGELSTAEDTER, C. LUO, A. SEALY, P. ARTAXO, C. BENITEZ-NEILSON, S.
820 BONNET, Y. CHEN, P. Y. CHUANG, D. D. COHEN, F. DULAC, B. HERUT, A. M. JOHANSEN, N.
821 KUBILAY, R. LOSNO, W. MAENHAUT, A. PAYTAN, J. A. PROSPERO, L. M. SHANK, and R. L.
822 SIEFERT (2009), Atmospheric Iron Deposition: Global Distribution, Variability, and
823 Human Perturbations, *Annu. Rev. Mar. Sci.*, *1*, 245-278.

824 MARTICORENA, B., and G. BERGAMETTI (1995), Modeling the atmospheric dust cycle: 1. Design of
825 a soil-derived dust emission scheme, *Journal of Geophysical Research: Atmospheres*,
826 *100*(D8), 16415-16430, doi=10.1029/95JD00690.

827 MENUT, L. (2008), Sensitivity of hourly Saharan dust emissions to NCEP and ECMWF
828 modeled wind speed, *J. Geophys. Res.*, *113*, D16201, doi:10.1029/2007JD009522.

829 MORCRETTE, J. J., A. BELJAARS, A. BENEDETTI, L. JONES, and O. BOUCHER: Sea-salt and dust
830 aerosols in the ECMWF IFS model, *Geophys. Res. Lett.*, *35*, L24813,
831 doi:10.1029/2008GL036041, 2008.

832 Morcrette, J. J., O. Boucher, L. Jones, D. Salmond, P. Bechtold, A. Beljaars, A. Benedetti, A.
833 Bonet, J. W. Kaiser, M. Razinger, M. Schulz, S. Serrar, A. J. Simmons, M. Sofiev, M.
834 Suttie, A. M. Tompkins, and A. Untch: Aerosol analysis and forecast in the European
835 Centre for Medium-Range Weather Forecasts Integrated Forecast System: Forward
836 modeling, *J. Geophys. Res.-Atmos.*, 114, D06206, doi: 10.1029/2008JD011235, 2009.

837 Nickovic, S., G. Kallos, A. Papadopoulos, and O. Kakaliagou (2001), A model for prediction
838 of desert dust cycle in the atmosphere, *Journal of Geophysical Research: Atmospheres*,
839 *106*(D16), 18113-18129, doi=10.1029/2000JD900794.

840 Ozer, P., M. Laghdaf, S. O. M. Lemine, and J. Gassani (2007), Estimation of air quality
841 degradation due to Saharan dust at Nouakchott, Mauritania, from horizontal visibility
842 data, *Water Air and Soil Pollution*, *178*(1-4), 79-87.

843 Pérez, C., Nickovic, S., Pejanovic, G., Baldasano, J.M., Özsoy, E. (2006a), Interactive dust-
844 radiation modeling: a step to improve weather forecast. *Journal of Geophysical*
845 *Research*, 111, D16206. doi:10.1029/2005JD006717.

846 Pérez, C., S. Nickovic, J. M. Baldasano, M. Sicard, F. Rocadenbosch, and V. E. Cachorro
847 (2006b), A long Saharan dust event over the western Mediterranean: Lidar, Sun
848 photometer observations, and regional dust modeling, *Journal of Geophysical Research:*
849 *Atmospheres*, *111*(D15), D15214, doi=10.1029/2005JD006579.

850 Pérez, C., K. Haustein, Z. Janjic, O. Jorba, N. Huneus, J. M. Baldasano, T. Black, S. Basart,
851 S. Nickovic, R. L. Miller, J. P. Perlwitz, M. Schulz, and M. Thomson (2011),
852 Atmospheric dust modeling from meso to global scales with the online NMMB/BSC-
853 Dust model - Part 1: Model description, annual simulations and evaluation, *Atmos.*
854 *Chem. Phys.*, *11*(24), 13001-13027, doi=10.5194/acp-11-13001-2011.

855 Pérez García-Pando, C., Stanton, M., Diggle, P., Trzaska, S., Miller, R. L., Perlwitz, J. P.,
856 Baldasano, J. M., Cuevas, E., Ceccato, P., Yaka, P., and Thomson, M. (2014a). Soil dust

857 aerosols and wind as predictors of seasonal meningitis incidence in niger.
858 *Environmental Health Perspectives*, 122, 679–686. doi:10.1289/ehp.1306640.

859 Pérez García-Pando, C., M.C. Thomson, M. Stanton, P. Diggle, T. Hopson, R. Pandya, and
860 R.L. Miller (2014b): Meningitis and climate: From science to practice. *Earth*
861 *Perspectives.*, 1, 14, doi:10.1186/2194-6434-1-14.

862 Pey, J., X. Querol, A. Alastuey, F. Forastiere, and M. Stafoggia (2013), African dust
863 outbreaks over the Mediterranean Basin during 2001-2011: PM10 concentrations,
864 phenomenology and trends, and its relation with synoptic and mesoscale meteorology,
865 *Atmos. Chem. Phys.*, 13(3), 1395-1410, doi=10.5194/acp-13-1395-2013.

866 Querol, X., J. Pey, M. Pandolfi, A. Alastuey, M. Cusack, N. Pérez, T. Moreno, M. Viana, N.
867 Mihalopoulos, G. Kallos, and S. Kleanthous (2009), African dust contributions to mean
868 ambient PM10 mass-levels across the Mediterranean Basin, *Atmospheric Environment*,
869 43(28), 4266-4277, doi=http://dx.doi.org/10.1016/j.atmosenv.2009.06.013.

870 Reid, J. S., A. Benedetti, P. R. Colarco, and Hansen, J. A.: International Operational Aerosol
871 Observability Workshop, *Bull. Amer. Meteorol. Soc.*, 92, ES21-ES24,
872 doi=10.1175/2010bams3183.1, 2011.

873 Remer, L. A., Y. J. Kaufman, D. Tanre, S. Mattoo, D. A. Chu, J. V. Martins, R. R. Li, C.
874 Ichoku, R. C. Levy, R. G. Kleidman, T. F. Eck, E. Vermote, and B. N. Holben (2005),
875 The MODIS aerosol algorithm, products, and validation, *Journal of the Atmospheric*
876 *Sciences*, 62(4), 947-973.

877 Rienecker, M. M., Suarez, M. J., Gelaro, R., Todling, R., Bacmeister, J., Liu, E., Bosilovich,
878 M. G., Schubert, S. D., Takacs, L., Kim, G.-K., Bloom, S., Chen, J., Collins, D., Conaty,
879 A., da Silva, A, Gu, W., Joiner, J., Koster, R. D., Lucchesi, R., Molod, A., Owens, T.,
880 Pawson, S., Pegion, P., Redder, C. R., Reichle, R., Robertson, F. R., Ruddick, A. G.,
881 Sienkiewicz, M., and Woollen, J.: MERRA: NASA's Modern-Era Retrospective

882 Analysis for Research and Applications. *J. Climate*, 24, 3624-3648, doi:10.1175/JCLI-
883 D-11-00015.1, 2011.

884 Ryder, C. L., Highwood, E. J., Rosenberg, P. D., Trembath, J., Brooke, J. K., Bart, M., ...
885 Washington, R. (2013). Optical properties of Saharan dust aerosol and contribution from
886 the coarse mode as measured during the Fennec 2011 aircraft campaign. *Atmospheric*
887 *Chemistry and Physics*, 13(1), 303–325. doi:10.5194/acp-13-303-2013

888 Sandu I, Beljaars A, Bechtold P, Mauritsen T, Balsamo G, Why is it so difficult to represent
889 stably stratified conditions in numerical weather prediction (NWP) models? (2013),
890 *Journal of Advances in Modeling Earth Systems* DOI 10.1002/jame.20013, URL
891 <http://dx.doi.org/10.1002/jame.20013>.

892 Schroedter-Homscheidt, M., Oumbe, A., Benedetti, A., & Morcrette, J.-J. (2013). Aerosols
893 for Concentrating Solar Electricity Production Forecasts: Requirement Quantification
894 and ECMWF/MACC Aerosol Forecast Assessment. *Bulletin of the American*
895 *Meteorological Society*, 94(6), 903–914. doi:10.1175/BAMS-D-11-00259.1.

896 Schulz, M., Prospero, J. M., Baker, A. R., Dentener, F., Ickes, L., Liss, P. S., Mahowald, N.
897 M., Nickovic, S., Pérez, C., Rodríguez, S., Manmohan Sarin, M., Tegen, I., and Duce,
898 R. A., (2012). Atmospheric transport and deposition of mineral dust to the ocean:
899 implications for research needs. *Environmental Science & Technology*, 46, 10390–404.
900 doi:10.1021/es300073u.

901 Shao, Y., Raupach, M. R., and Findlater, P. A.: Effect of saltation bombardment on the
902 entrainment of dust by wind. *J. Geophys. Res.*, 98, 12719-12726
903 doi:10.1029/93JD00396, 1993.

904 Shao, Y., Y. Yang, J. Wang, Z. Song, L. M. Leslie, C. Dong, Z. Zhang, Z. Lin, Y. Kanai, S.
905 Yabuki, and Chun, Y.: Northeast Asian dust storms: Real-time numerical prediction and

906 validation, *Journal of Geophysical Research: Atmospheres*, 108, 4691,
907 doi=10.1029/2003JD003667, 2003.

908 Sokolik, I. N., D. M. Winker, G. Bergametti, D. A. Gillette, G. Carmichael, Y. J. Kaufman, L.
909 Gomes, L. Schuetz, and J. E. Penner (2001), Introduction to special section: Outstanding
910 problems in quantifying the radiative impacts of mineral dust, *J. Geophys. Res.-Atmos.*,
911 106(D16), 18015-18027

912 Tegen, I. (2003), Modeling the mineral dust aerosol cycle in the climate system, *Quaternary*
913 *Science Reviews*, 22(18-19), 1821-1834

914 Terradellas, E., Baldasano, J.M., Cuevas, E., Basart, S., Huneus, N., Camino, C., Dundar, C.,
915 and Benincasa, F.: Evaluation of atmospheric dust prediction models using ground-
916 based observations, in: EGU General Assembly Conference, 7–12 April 2013, Vienna,
917 Austria, Abstracts, Vol. 15, p. 8274, 2013.

918 Textor, C., M. Schulz, S. Guibert, S. Kinne, Y. Balkanski, S. Bauer, T. Berntsen, T. Berglen,
919 O. Boucher, M. Chin, F. Dentener, T. Diehl, R. Easter, H. Feichter, D. Fillmore, S.
920 Ghan, P. Ginoux, S. Gong, J. E. Kristjansson, M. Krol, A. Lauer, J. F. Lamarque, X.
921 Liu, V. Montanaro, G. Myhre, J. Penner, G. Pitari, S. Reddy, O. Seland, P. Stier, T.
922 Takemura, and X. Tie (2006), Analysis and quantification of the diversities of aerosol
923 life cycles within AeroCom, *Atmos. Chem. Phys.*, 6, 1777-1813

924 Vogel, B., Vogel, H., Bäumer, D., Bangert, M., Lundgren, K., Rinke, R., and Stanelle, T.
925 (2009), The comprehensive model system COSMO-ART – Radiative impact of aerosol
926 on the state of the atmosphere on the regional scale, *Atmos. Chem. Phys.*, 9, 8661-8680,
927 doi:10.5194/acp-9-8661-2009.

928 Washington, R., Flamant, C., Parker, D. J., Marsham, J., McQuaid, J. B., Brindley, H., Todd,
929 M., Highwood, E. J., Chaboureau, J.-P., Kocha, C., Bechir, M., Saci, A., and Ryder, C.
930 L. (2013), Fennec –The Saharan Climate System, submitted to CLIVAR Exchanges.

931 Winker, D. M., M. A. Vaughan, A. Omar, Y. Hu, K. A. Powell, Z. Liu, W. H. Hunt, and S. A.
932 Young (2009), Overview of the CALIPSO Mission and CALIOP Data Processing
933 Algorithms, *Journal of Atmospheric and Oceanic Technology*, 26(11), 2310-2323,
934 doi=10.1175/2009jtecha1281.1.

935 Woodward, S. (2001), Modeling the atmospheric life cycle and radiative impact of mineral
936 dust in the Hadley Centre climate model, *Journal of Geophysical Research:*
937 *Atmospheres*, 106(D16), 18155-18166, doi=10.1029/2000JD900795.

938 Woodward, S. (2011), Mineral dust in HadGEM2, Hadley Centre Technical, Note 87, Met
939 Office Hadley Centre, Exeter, Devon, UK.

940 Zhou, C. H., S. L. Gong, X. Y. Zhang, Y. Q. Wang, T. Niu, H. L. Liu, T. L. Zhao, Y. Q.
941 Yang, and Q. Hou (2008), Development and evaluation of an operational SDS
942 forecasting system for East Asia: CUACE/Dust, *Atmos. Chem. Phys.*, 8(4), 787-798,
943 doi=10.5194/acp-8-787-2008.

944

945

946

Dust model	Domain	Meteo. initial fields	Texture and vegetation type datasets	Radiation Interaction with dust	Horiz./Vert. resolution	Dust Emission Scheme	Surface wind speed for dust emission	Threshold friction velocity	Dry and wet deposition	Transport size bins
BSC-DREAM8b	Regional	NCEP	STATSGO-FAO 5 min USGS 1 km	P06	0.3°x0.3° 24 σ -layers	S93	viscous sublayer	B41 F99	Z01 N01	8 bins 0.1-10 μ m
NMMB/BSC-Dust	Regional/	NCEP	STATSGO-FAO 5 min USGS 1 km	no	0.25°x0.25° 40 σ -layers	W79-MB95	viscous sublayer	IW82 F99	Z01 BMJ	8 bins 0.1-10 μ m
ECMWF/MACC	Global	ECMWF	USGS 1km	no	1°x1° 91 layers	GP88-G01	10m gusts from 10m wind field	G01	B02 GC86	3 bins 0.03-20 μ m
MetUM™	Global	MetUM	FOA 2009	no	0.35°x0.23° 70 layers	W01, W11	10m wind field	B41 F99	W01	2 bins 0.1-10 μ m
DREAM8-NMME	Regional	ECMWF	STATSGO-FAO 5 min USGS 1 km	no	0.2°x0.2° 28 σ -layers	S93	viscous sublayer	B41 F99	Z01 N01	8 bins 0.1-10 μ m

947 **Table 1** : Summary of the main features of each model included in the present contribution.

948 The codes denote the following references. B02: Boucher et al. (2002); B41: Bagnold (1941); F99: Fécan et al. (1999); G01: Ginoux et al. (2001); GC86: Giorgi and
949 Chameides (1986); GP88: Gillette and Passi (1988); IW82: Iversen and White (1982); MB95: Marticorena and Bergametti (1995); S93: adapted Shao et al. (1993), P06: Pérez
950 et al. (2006a); White (1979); Z01: Zhang et al. (2001); N01: Nickovic et al. (2001); W01: Woodward (2001); W11: Woodward (2011).

	Southern Europe			Central Europe			Northern Europe		
	24	48	72	24	48	72	24	48	72
DREAM8-NMME	0,18	0,21	0,18	0,13	0,14	0,15	0,19	0,19	0,20
BSC-DREAM8b	0,20	0,20	0,19	0,17	0,17	0,16	0,32	0,33	0,31
ECMWF/MACC-Dust	0,18	0,17	0,24	0,15	0,14	0,14	0,12	0,18	0,12
NMMB_BSC	0,19	0,21	0,23	0,17	0,16	0,17	0,23	0,26	0,25
MetUM	0,12	0,14	0,14	0,15	0,16	0,15	0,18	0,18	0,24

951 **Table 2:** Root mean square (RMS) error quantifying the performance to reproduce AERONET total AOD for
952 each model. The statistics are computed for stations in Southern, Central and Northern Europe (Fig. 1),
953 considering the period between the 5th and 11th of April. We note that for all models the dust AOD was used.

954

955

	Southern Europe			Central Europe			Northern Europe		
	24	48	72	24hr	48	72	24hr	48	72
DREAM8-NMME	-0,10	-0,10	-0,09	-0,06	-0,06	-0,06	-0,06	-0,07	-0,06
BSC-DREAM8b	-0,09	-0,10	-0,08	-0,10	-0,10	-0,08	-0,22	-0,22	-0,20
ECMWF/MACC-Dust	0,09	0,07	0,08	-0,07	-0,07	-0,06	-0,06	-0,07	-0,05
NMMB_BSC	-0,11	-0,11	-0,08	-0,10	-0,10	-0,10	-0,13	-0,15	-0,11
MetUM	0,04	0,06	0,02	-0,06	-0,06	-0,04	-0,03	-0,04	-0,03

956 **Table 3:** Same as Table 2 but for mean bias (MB).

957

958

	Southern Europe			Central Europe			Northern Europe		
	24	48	72	24hr	48	72	24hr	48	72
DREAM8-NMME	0,76	0,62	0,74	0,50	0,42	0,21	0,74	0,75	0,67
BSC-DREAM8b	0,66	0,66	0,66	0,17	0,11	0,04	0,64	0,63	0,48
ECMWF/MACC-Dust	0,83	0,81	0,69	0,29	0,37	0,41	0,91	0,78	0,91
NMMB_BSC	0,72	0,64	0,61	0,14	0,24	0,11	0,76	0,54	0,47
MetUM	0,89	0,87	0,81	0,20	0,12	0,17	0,72	0,73	0,43

959 **Table 4:** Same as Table 2 but for Pearson correlation coefficient (R).

960

961

	RMS			Mean Bias			Correlation		
	24	48	72	24	48	72	24	48	72
DREAM8-NMME	15,9	17,1	16,6	-0,4	-2,1	-1,8	0,22	0,13	0,15
BSC-DREAM8b	28,6	27,3	28,8	12,0	11,7	12,7	0,38	0,41	0,35
ECMWF/MACC-Dust	28,1	28,9	28,6	20,2	20,7	20,1	0,36	0,34	0,47
NMMB_BSC	16,8	16,0	15,2	-9,9	-9,6	-7,6	0,46	0,55	0,53
MetUM	147,1	126,5	125,1	110,7	99,0	100,4	0,29	0,35	0,38

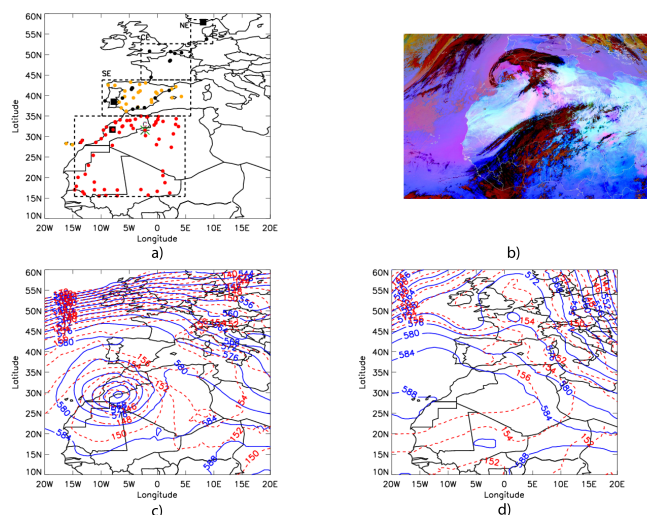
962 **Table 5:** Root mean square (RMS) error, mean bias and correlation quantifying the performance to reproduce
963 dust surface concentration in the Iberian Peninsula. Figure 1 illustrates the location of the stations used in the
964 computation of the statistics. We note that for the models, the total dust surface concentration was used.

965

966

	AOD			Sfc. Conc.		
	24	48	72	24	48	72
DREAMS-NMME	0,35	0,37	0,34	1,06	0,99	0,98
BSC-DREAM8b	0,41	0,44	0,43	1,91	1,86	1,88
ECMWF/MACC-Dust	0,50	0,50	0,62	2,28	2,36	1,96
NMMB_BSC	0,45	0,48	0,48	0,75	0,67	0,71
MetUM	0,34	0,39	0,38	9,75	8,70	8,78

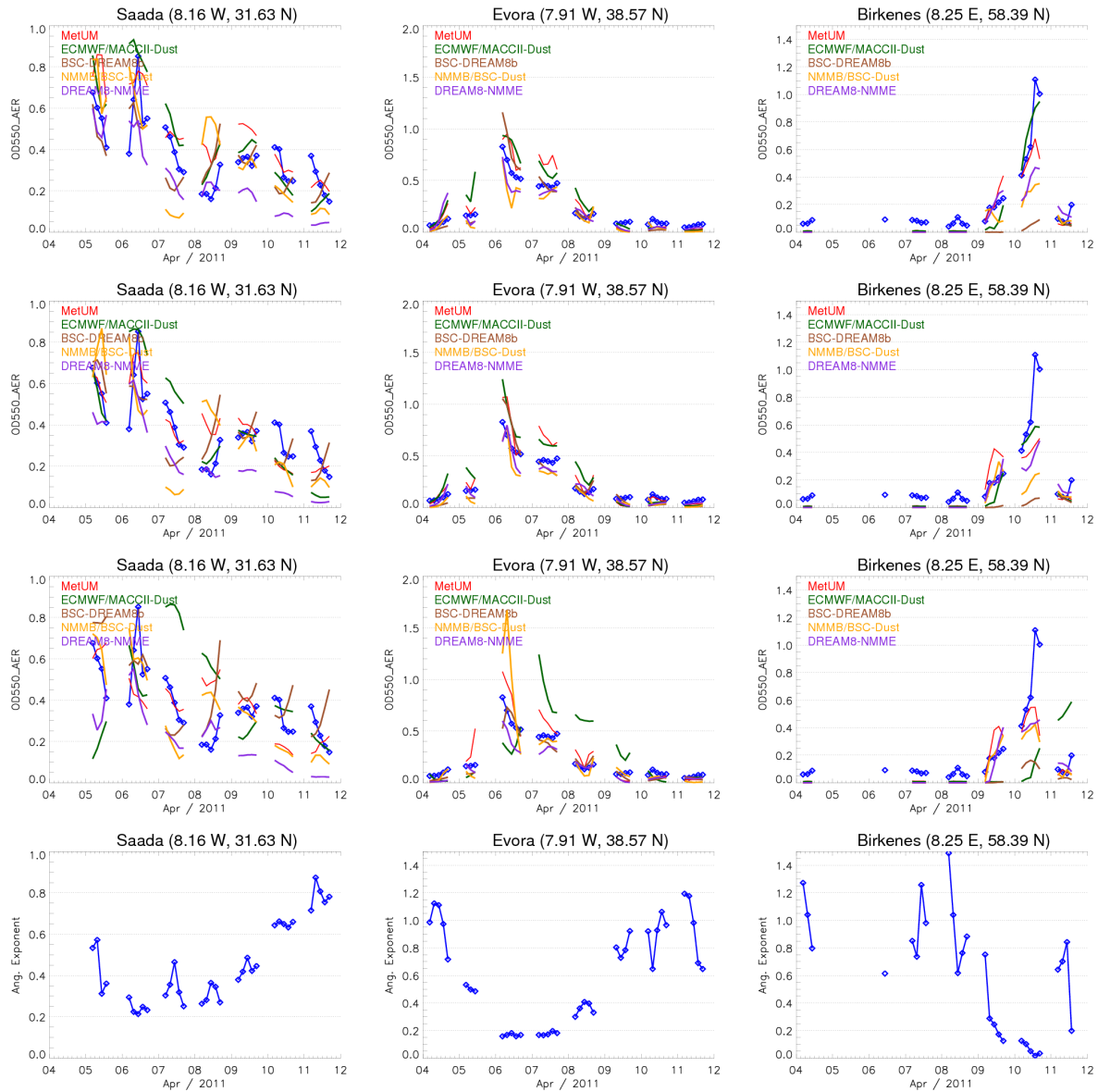
967 **Table 6:** Mean normalized gross error quantifying the performance to reproduce AERONET total AOD in
 968 Southern Europe and surface concentration for each model and each lead-time forecast. We note that for the
 969 models, the dust AOD and dust total surface concentrations were used.



970

971 **Figure 1:** (a) AERONET (orange), surface concentration (black), surface wind (green) and radiosounding
 972 (brown) stations used in this study are presented. Southern, Central and Northern Europe (SE, CE and NE,
 973 respectively as the dashed black squares) regions used in the statistical analysis are illustrated, as well as the
 974 region used to produce the emission time series in Figure 5. (b) The MSG/RGB dust product of the "spinning
 975 enhanced visible and infrared imager" (SEVIRI) shows the cloud band of the cyclone (red) and dust aerosol
 976 (pink) of the dust event over Northwest Africa on 5th April 2011 at 12:00. (c) Geopotential height at 500 hPa
 977 (blue lines) and (d) 850 hPa (red lines) for the 5th and 10th of April 2011 and wind field at 850 hPa.

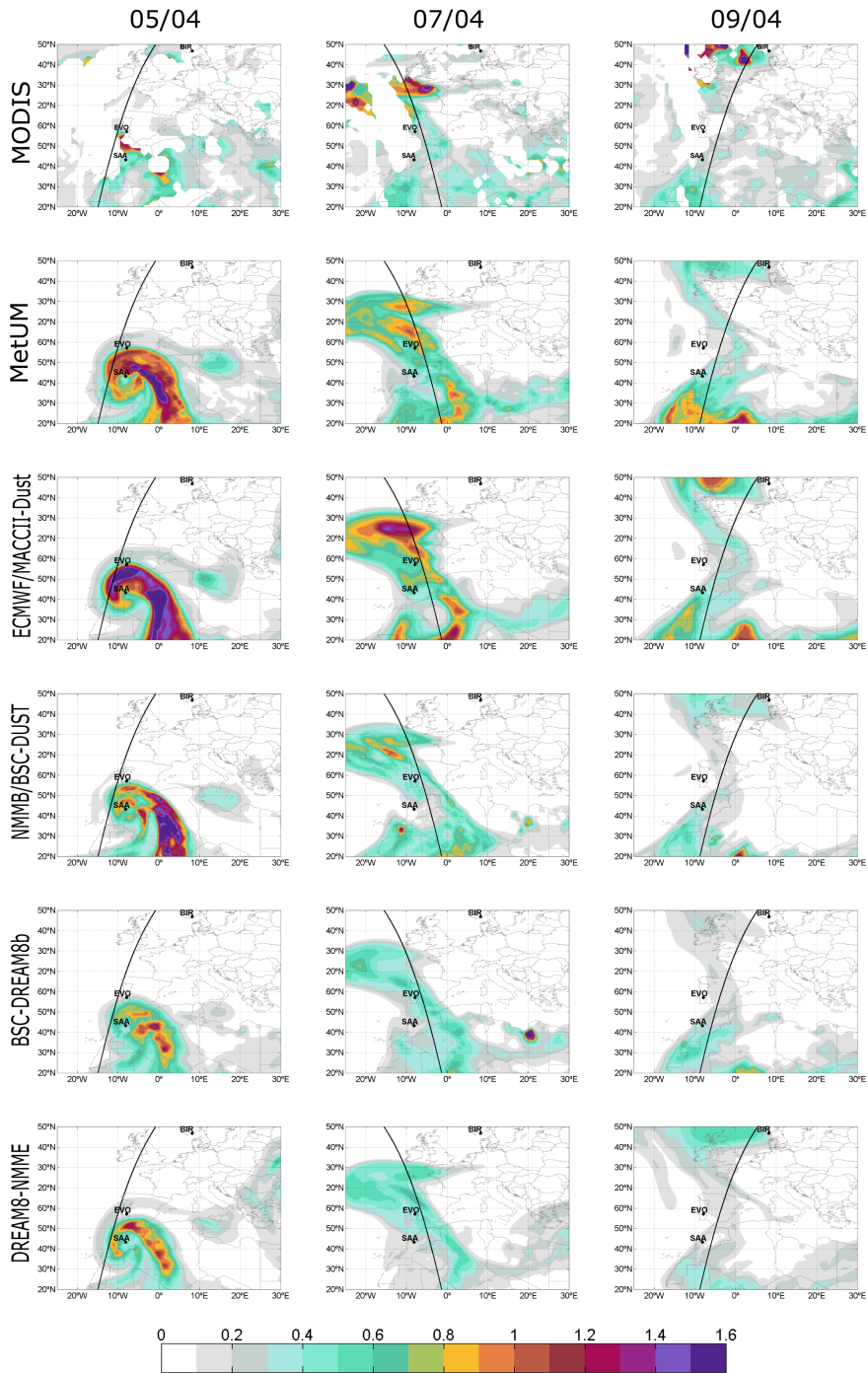
978



979

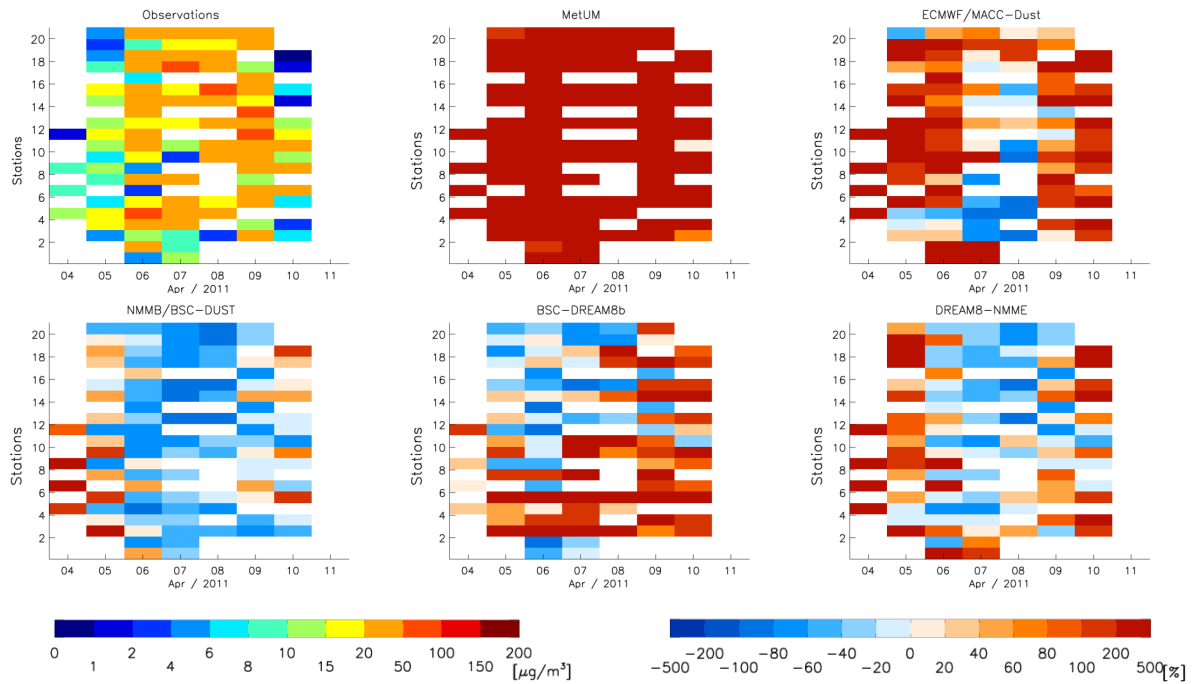
980 **Figure 2:** Total AOD at 550 nm at three selected sites from the AERONET network (blue line) and 24 (first
 981 row), 48 (second row) and 72 hr (third row) forecast of the model MetUM (red), ECMWF/MACC (green), BSC-
 982 DREAM8b (brown), NMMB/BSC-Dust (orange) and DREAM8-NMME (purple) are illustrated. The Angström
 983 exponent (dark blue dots) from the AERONET network at the three selected sites is included in the fourth row.
 984 Angström exponent <0.75 indicate the dominance of desert dust.

985



986

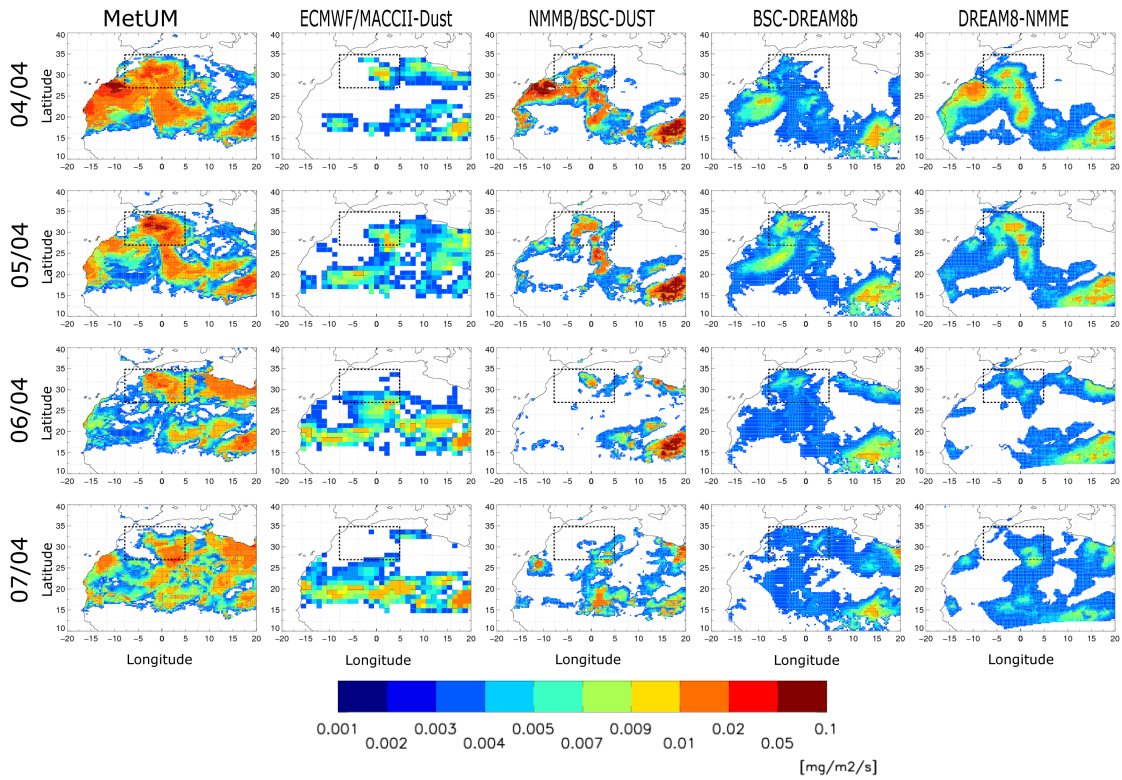
987 **Figure 3:** Maps of daily total AOD at 550 nm from MODIS (first row) and corresponding 24-hour forecast of
 988 models MetUM (second row), ECMWF/MACC (third row), NMMB/BSC-DUST (fourth row), BSC-DREAM8b
 989 (fifth row) and DREAM8-NMME (sixth row) for the 5th (first column), 7th (second column) and 9th (third
 990 column) of April 2011. Corresponding maps for all days between 4th and 11th of April are given in Figure S01 in
 991 the Supplement and 48 and 72-hour forecast maps are provided in Figure S02 and S03. The three AERONET
 992 site show in Fig. 2 (black dots) and the CALIPSO orbits (black lines) are also shown. The simulated AOD is
 993 computed as the average of the fields at 12 and 15 UTC.



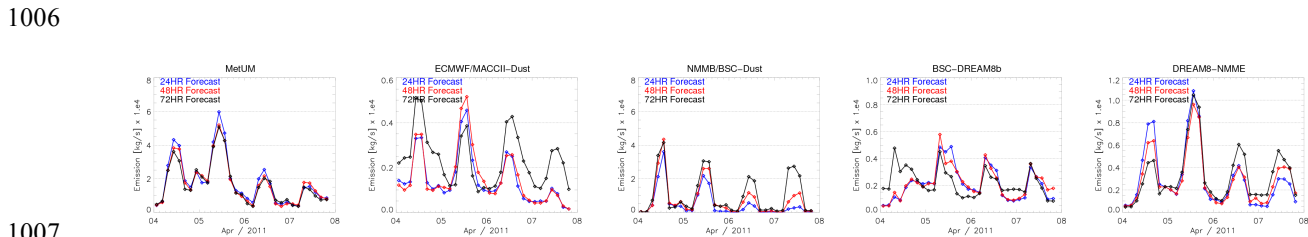
994

995 **Figure 4:** Daily measured surface concentration [$\mu\text{g m}^{-3}$] and normalized bias of corresponding 24 hour forecast
 996 surface concentration [%] at stations illustrated in Figure 1. Each row corresponds to one of the stations. Stations
 997 are ordered from south to north and white colour corresponds to days without measurements. Corresponding 24-
 998 hour forecast model surface concentration are illustrated in Figure S04 in the Supplement and the 48 and 72-hour
 999 of normalized bias of forecasted surface concentration are provided in Figure S05 and S06.

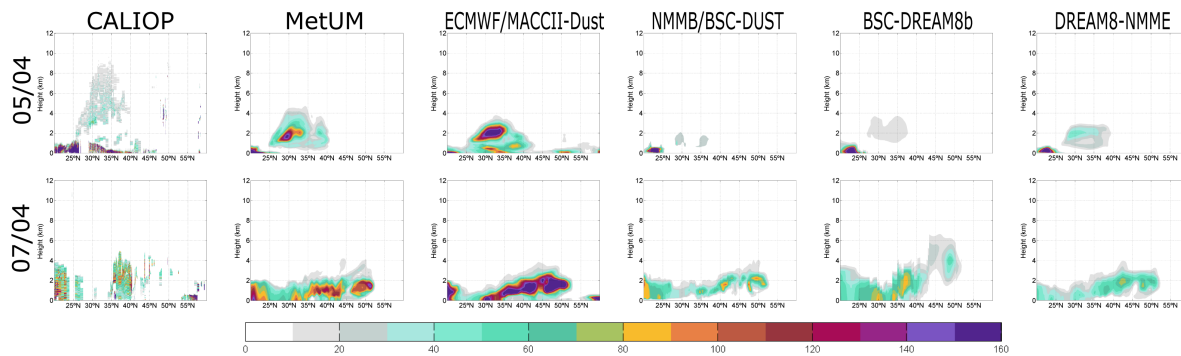
1000



1001
 1002 **Figure 5:** Forecasted daily average emission with 24-hour lead-time for the models MetUM (first column),
 1003 ECMWF/MACC (second column), NMMB/BSC-DUST (third row), BSC-DREAM8b (forth column) and
 1004 DREAM8-NMME (fifth row). Dashed box illustrates region used in the time series emissions illustrated in
 1005 Figure 6.



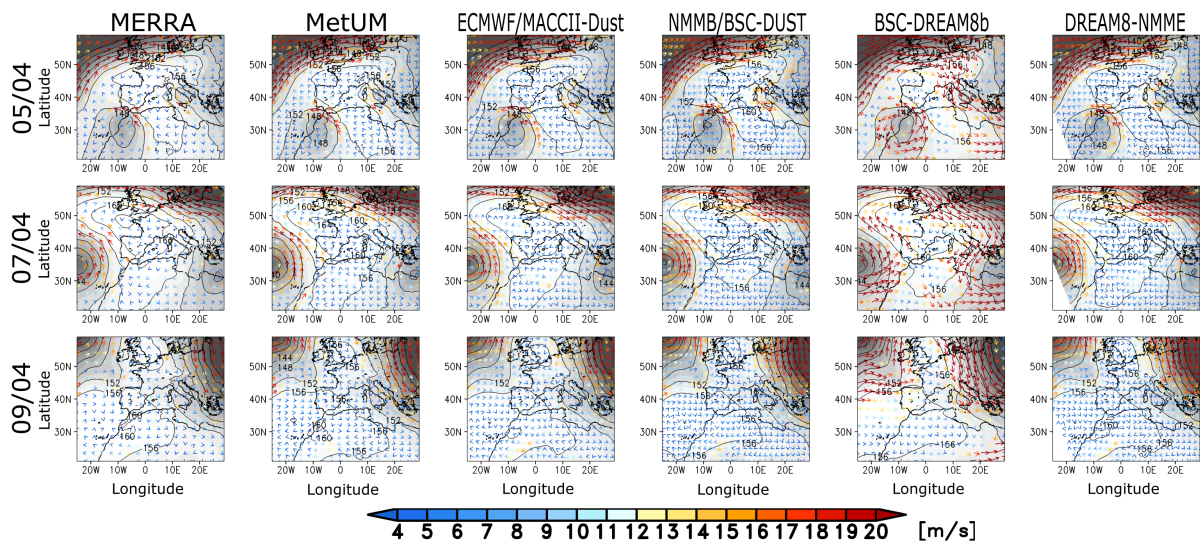
1007
 1008 **Figure 6:** Time series of 3 hourly emissions from models MetUMTM, ECMWF/MACC, NMMB/BSC-Dust,
 1009 BSC-DREAM8b and DREAM8-NMME with 24, 48 and 72 hours lead-time (blue, red and black respectively).



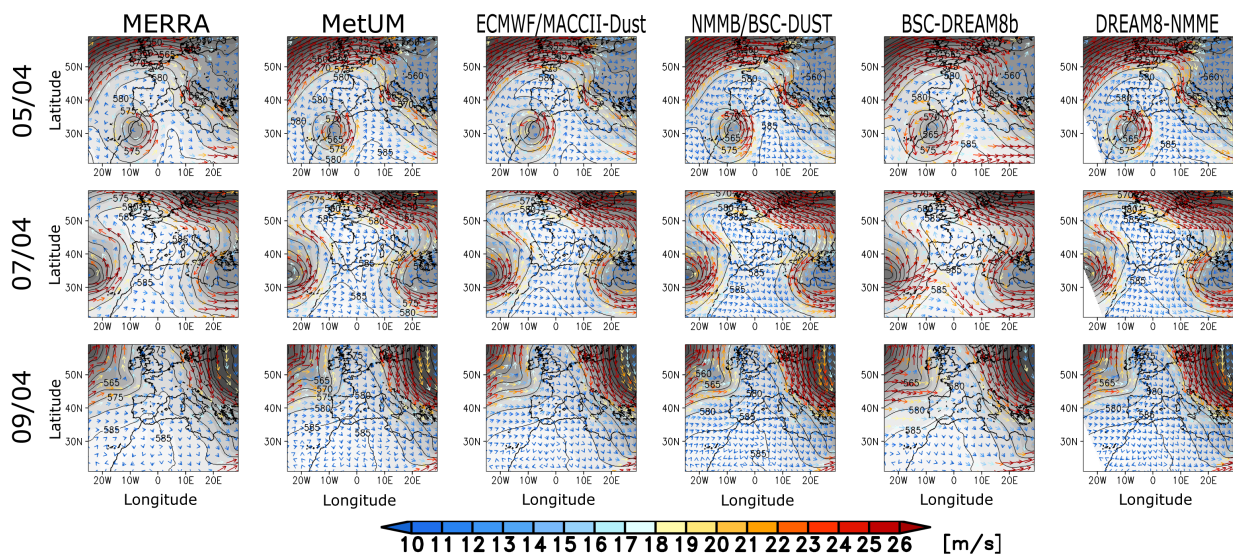
1011

46

1012 **Figure 7:** Profiles of measured total extinction coefficient at 532 nm from the CALIOP instrument onboard of
 1013 the CALIPSO satellite and 24 hour forecasted dust extinction coefficient profiles at 532 nm from models
 1014 MetUM, ECMWF/MACC, NMMB/BSC-DUST, BSC-DREAM8b and DREAM8-NMME. Conditions are
 1015 presented for the 5th (upper row) and 7th (lower row) of April. Overpass of the satellite in each case is illustrated
 1016 in Figure 3. Corresponding forecasted model profiles for 48 and 72 hours lead times are illustrated in Figure S10
 1017 and S11, respectively)
 1018



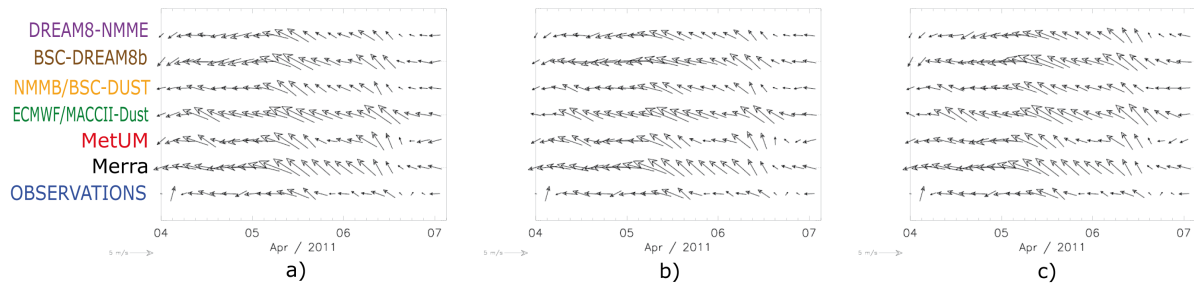
1019
 1020 **Figure 8:** The geopotential height (grey shaded with contour labels in gpdm) and wind speed stream lines at 850
 1021 hPa on 5th (first row), 7th (second row) and 9th (third row) of April 2011 at 12 UTC from MERRA reanalysis and
 1022 the 24 hour forecast from MetUM, ECMWF/MACC, NMMB/BSC-DUST, BSC-DREAM8b and DREAM8-
 1023 NMME (from left to right).



1024
 1025

1026 **Figure 9:** Same as Figure 8 but for 500 hPa.

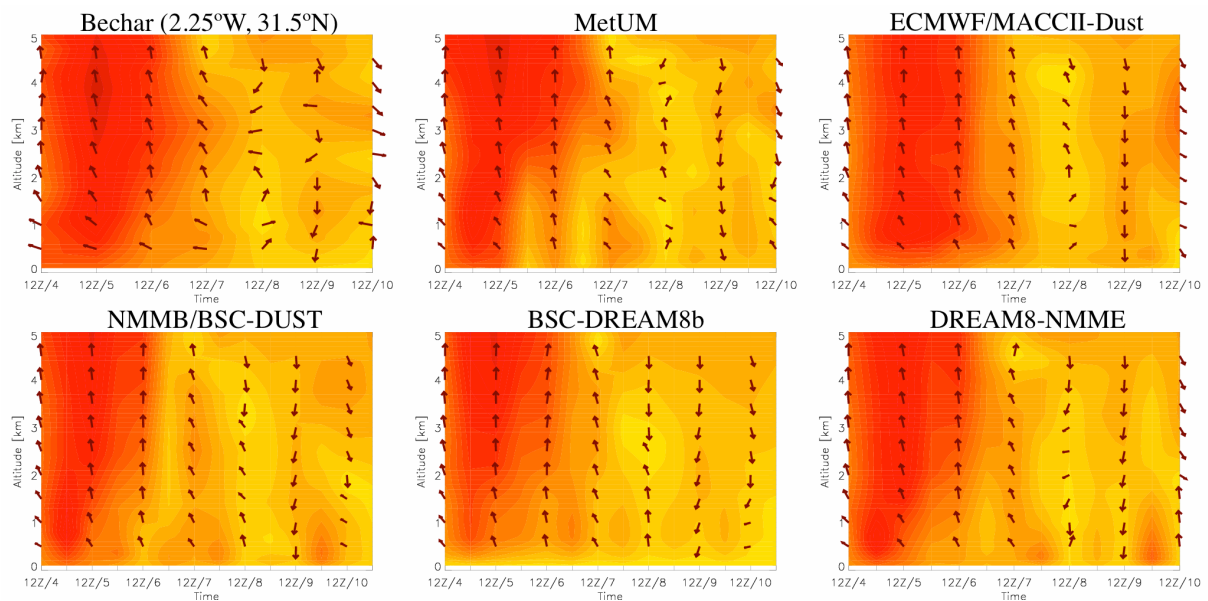
1027



1028

1029 **Figure 10:** Time series of near-surface wind speeds in dust source region. Three-hourly values of the 10m-wind
1030 speed from observations and re-analysis (MERRA), global models and regional models for the period 4 Apr
1031 2011 to 7 Apr 2011 with (a) 24 hours lead time, (b) 48 hours, and (c) 72 hours. Observations are averaged over
1032 the region illustrated in Figure 1. The 10m-winds from the models are averaged over the grid boxes enclosing the
1033 observation station.

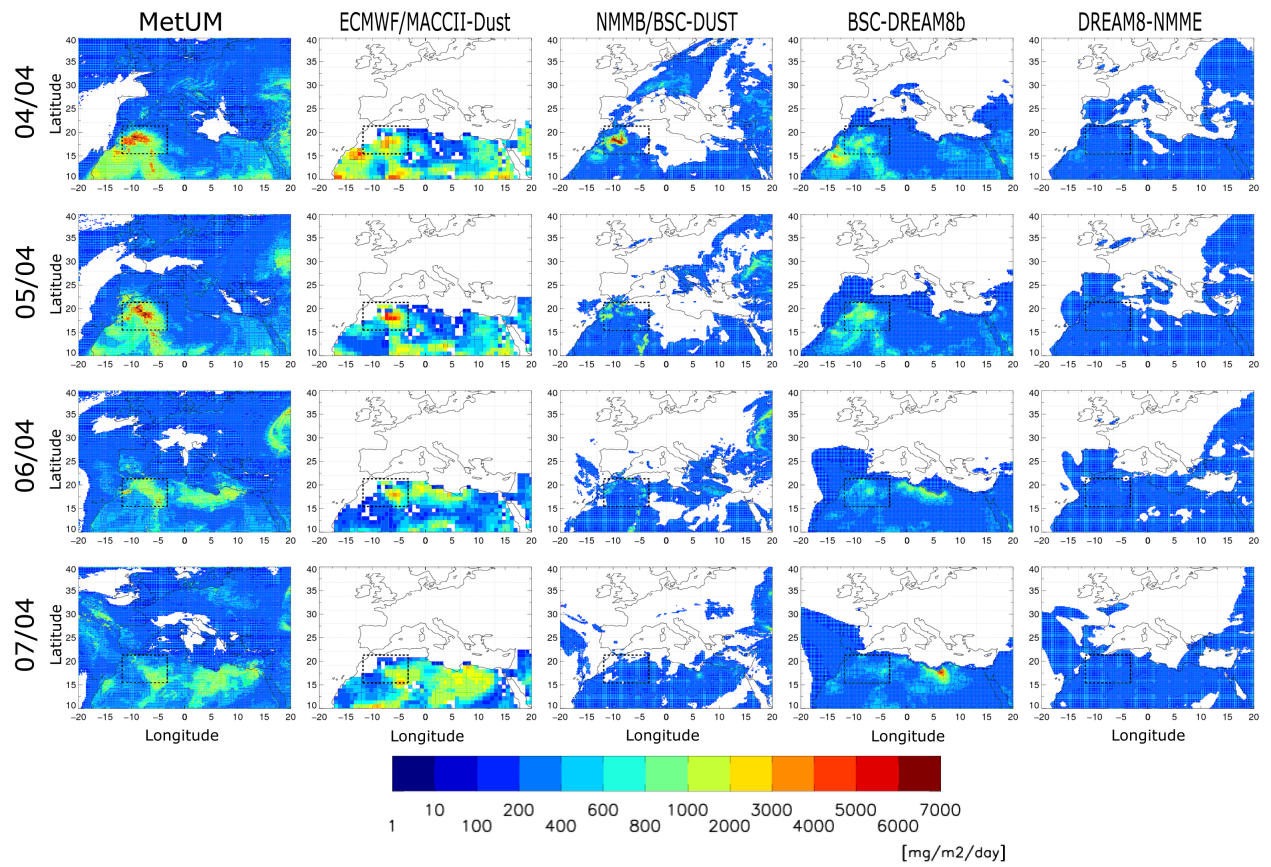
1034



1035

1036 **Figure 11:** Profiles of measured wind speed (m/s, filled contours) and direction (vectors, first column) between
1037 the 4th and 10th of April from radiosounding at Bachar (2.25°W, 31.5°N; first row) and the corresponding 24-
1038 hour forecast of models MetUM, ECMWF/MACC, NMMB/BSC-DUST, BSC-DREAM8b and DREAM8-
1039 NMME.

1040



1041

1042 **Figure 12:** Total accumulated forecasted daily deposition with 24-hour lead time for the models MetUM,

1043 ECMWF/MACCI2-Dust, NMMB/BSC-DUST, BSC-DREAM8b and DREAM8-NMME (from left to right).